Stray Light Correction of the Marine Optical System

Michael E. Feinholz[1], Stephanie J. Flora[1], Mark A. Yarbrough[1], Keith R. Lykke[2], Steven W. Brown[2], B. Carol Johnson[2], and Dennis K. Clark[3]

[1]Moss Landing Marine Laboratories, Moss Landing, CA 95039
[2]National Institute of Standards and Technology, Gaithersburg, MD 20899
[3]Marine Optical Consulting, Arnold, MD 21012

Abstract

The Marine Optical System is a spectrograph-based sensor used in the Marine Optical Buoy for the vicarious calibration of ocean color satellite sensors. It is also deployed from ships in instruments used to develop bio-optical algorithms that relate the optical properties of the ocean to its biological content. In this work, an algorithm is applied to correct the response of the Marine Optical System for scattered, or improperly imaged, light in the system. The algorithm, based on the measured response of the system to a series of monochromatic excitation sources, reduces the effects of scattered light on the measured source by one to two orders of magnitude. Implications for the vicarious calibration of satellite ocean color sensors and the development of bio-optical algorithms are described. The algorithm is a one-dimensional point spread correction algorithm, generally applicable to non-imaging sensors, but can in principle be extended to higher dimensions for imaging systems.

Keywords: calibration, ocean color, point-spread response, radiometry, spectrograph, stray light

1. Introduction

The optical properties of seawater reflect its composition. Under natural illumination from sunlight, radiometric measurements of the light leaving the ocean contain information about the nature and concentration of dissolved and suspended materials. The optical properties of the ocean can be related to meaningful physical and biogeochemical data products such as the concentration of phytoplankton chlorophyll-*a* through bio-optical algorithms. Quantitative measurements of global ocean radiance distributions by satellite sensors can yield a variety of relevant information regarding the state of the world's oceans. For example, phytoplankton use carbon dioxide from the ocean/atmosphere system to conduct photosynthesis and understanding this interaction is important to climate research. Additionally, satellite observations are used to produce global assays of biomass and carbon cycling in the world's oceans; this information provides a more accurate understanding of the Earth's carbon balance and the relationship between the ocean's productivity and the Earth's climate.

Multi-sensor, multi-year measurements are required to develop an understanding of the state of the world's oceans and their response to environmental changes. Of particular interest are measurements of oceanic ecosystem changes attributable to anthropogenic origins. Meaningful synthesis of measurements from multiple sensors over decadal time scales into a coherent picture of the evolution of the Earth's oceans requires a detailed understanding of the sources of uncertainty in those measurements. Radiometric quantities of interest in ocean color research include the water-leaving spectral radiance $L_w(\lambda)$, the down-welling spectral irradiance incident at the sea surface,

$E_s(\lambda)$, and remote sensing reflectance, $R_{RS}(\lambda) = L_W(\lambda)/E_S(\lambda)$ (Mueller and Austin 2002).

The radiometric uncertainty goal for water-leaving radiance, $L_w(\lambda)$, determined from satellite ocean color data, as adopted by the National Aeronautics and Space Administration (NASA), is a relative combined standard uncertainty[1] of 5 % for open ocean waters where the dominant interaction is absorption by phytoplankton pigments (Hooker et al. 1993; Mueller and Austin 2002). A 5 % uncertainty in $L_w(\lambda)$ results in an uncertainty of 35 % in the concentration of phytoplankton chlorophyll-*a* derived from bio-optical algorithms (Gordon 1987). Because the $L_w(\lambda)$ component in the blue spectral region, for clear open-ocean water is typically about 10 % of the total at-satellite radiance, the satellite should be calibrated with an uncertainty of about 0.5 % to achieve an uncertainty of 5 % in $L_w(\lambda)$. Absolute calibration uncertainties in the visible for ocean color sensors are approximately 5 % (Guenther et al. 1996; Johnson et al. 1999). Consequently, to obtain the accuracies required to support the science data requirements, ocean color satellites are calibrated vicariously using accurate and continuous measurements of $L_w(\lambda)$ with ocean-based instruments combined with methods to estimate the atmospheric contribution to the at-satellite radiance in the ocean color bands (Gordon 1998).

The primary reference instrument for most ocean color satellites, including the U. S. Moderate Resolution Imaging Spectroradiometer (MODIS) and Sea-Viewing Wide

[1] In this document, the term "combined standard uncertainty" refers to the combination in quadrature of the Type A "standard uncertainty", as determined from the standard deviation of the measured data itself, with any Type B

Field-of-View Sensor (SeaWiFS), is the Marine Optical Buoy (MOBY), a radiometric buoy stationed in the waters off Lanai, Hawaii (Fig. 1) (Clark et al. 2003). MOBY measures up-welling radiance L_u as well as the down-welling irradiance E_d at different depths in the ocean using a hyperspectral instrument known as the Marine Optical System (MOS) (Fig. 2). MOS detects radiation over the spectral range from 350 nm to 955 nm, and is located in the instrument bay at the bottom of MOBY. MOS is fiber-optically connected to radiance and irradiance ports on the three MOBY arms (denoted Top, Mid, and Bot, typically at 1 m, 5 m and 9 m depths), as well as a surface irradiance port and an up-welling radiance port at the bottom of the buoy. A typical set of up-welling radiance data from MOBY is shown in Fig. 3. As described in Clark et al. (2003), these data are used to determine the water-leaving radiance, L_w.

Because each satellite sensor has a different set of channel filter functions, they must either generate their own bio-optical algorithm or transform their measurements to conform to a standard bio-optical algorithm (O'Reilly et al. 1998). Development of a high resolution, hyperspectral ocean color/data product database would enable bio-optical algorithms to be developed for each satellite sensor, placing all measured data products on a common platform. The MOS sensor is used in two shipboard deployable systems involved in the development of a hyperspectral ocean color data base, a profiling system known as the MOS Profiler and a Remotely Operated Vehicle system known as the MOS ROV (Yarbrough et al. 2007). The MOS Profiler, shown in Fig. 4, is deployed from a ship using a tethered winch to measure the down-welling irradiance and the up-welling

---

uncertainties determined using models or other external information. The combined standard uncertainty is given the symbol u_c, and an "expanded uncertainty" is denoted $k \cdot u_c$. (Taylor and Kuyatt 1994)

radiance at different depths in the ocean. The ROV is a fiber-coupled system designed to limit effects of shadowing in its measurements (Fig. 5). The MOS interfaces with the ROV by way of fiber optic heads at the L_u and E_d ports, coupled to an above water E_s collector and a L_u fiber tip at the end of the ROV's sampling arm. With its small shadowing footprint and 0.1 m depth-control, the ROV is uniquely qualified to measure the near-surface up-welling radiance in turbid water. Equipped with a camera system and a fiber-coupled variable excitation system (both lasers and high-power LEDs), it is also used to characterize unique features in the ocean, for example coral fluorescence. Figure 6 shows representative data taken with the MOS Profiler during the Marine Optical Characterization Experiment 5 (MOCE-5) in Baja, Mexico (Flora et al. 2000). Interesting data from the MOS ROV are shown in Figure 7, including high-chlorophyll, turbid water data taken in the Chesapeake Bay, Maryland and coral fluorescence from Kaneohe Bay Hawaii. The spectra in figure 6 illustrate the approximate forty-times reduction in radiance near 450 nm (i.e. blue wavelength), versus relatively stable radiance near 550 nm (i.e. green), which is the basis of one bio-optical algorithm for phytoplankton chlorophyll-a concentration. Before development of the MOS ROV, near-surface upwelled radiance spectra in turbid waters (Fig. 7) were compromised by instrument self-shadowing with the large exterior dimensions of the MOS underwater housing.

The MOS system contains two single-grating spectrographs, a blue spectrograph (BSG) to measure light in the near ultraviolet and visible region, from 340 nm to 640 nm, and a red spectrograph (RSG) to measure light in the red and near infrared spectral region, from 550 nm to 955 nm (Clark et al. 2002). The detector used in both

spectrographs is a 512 by 512 element, thermoelectrically cooled, charge-coupled device (CCD). Optics relay light from one of two ports on the MOS housing through a dichroic mirror to the blue and red spectrographs, respectively. Independent shutters allow different integration times for the two spectrographs to maximize the dynamic range of the system. A long pass filter in the red spectrograph eliminates possible second order diffraction effects.

Spectrographs are imaging systems with dispersive elements and multi-element detectors that enable simultaneous acquisition of an entire spectrum over some finite spectral width. There are intrinsic limitations in the image quality in these instruments. There is a finite signal originating from radiation scattered from imperfections in the optical elements in the instrument. This unwanted signal from improperly imaged or scattered radiation, commonly referred to as stray light, is typically small — on the order of 0.01 % or less of the incident spectral radiant flux in a single grating spectrograph. However, it can give rise to unforeseen measurement errors when the spectral distribution of a source being measured differs significantly from the spectral distribution of the calibration source. This is a situation routinely encountered by MOS sensors, where they are calibrated against incandescent sources with a maximum radiance in the short-wave infrared and subsequently measure the up-welling radiance in the ocean, which peaks in the blue spectral region. Figure 8 shows a typical up-welling spectral radiance distribution measured by MOBY and the spectral radiance distribution of a NIST-traceable lamp-illuminated integrating sphere source.

Measurements with the two spectrographs in the MOS systems can be compared in the spectral interval from about 540 nm to 630 nm. Without consideration of stray

light, in this spectral range they give different values for L_u or E_d at a common wavelength. In Fig. 9, the L_u, uncorrected for stray light, is shown for the Top (Top), Middle (Mid) and Bottom (Bot) MOBY arms. The difference in the measured radiance in the overlap region is a function of depth, increasing for deeper lying MOBY arms. While the signal is small in this region (approximately 1 % of the peak radiance), the lack of agreement in the overlap region and particularly its dependence on the spectral distribution of the up-welling radiance are common manifestations of stray light in the system.

To look for stray light in MOS, the response of the two spectrographs in the MOS205 system to monochromatic laser excitation was measured. In this experiment, lasers were directed into an integrating sphere and the radiance was measured with each MOBY arm. For monochromatic radiation, the entrance slit is spatially imaged on the detector. Ideally, no radiation falls on detector elements outside the image. In practice, the image is modified by scattered light within the spectrograph and every element in the array can have a finite response to this monochromatic radiation. Results for the one spectrograph are shown in Fig. 10. The spectra are similar for both spectrographs. There are three components to the image: a strong sharp peak corresponding to the image of the spectrograph entrance slit on the CCD; a broad, peaked structure around the slit image; and a non-zero constant component. These three components are similar to specular, haze and diffuse components of reflectance (Kelley et al. 1998). The specular component corresponds to the properly imaged radiation; the haze and diffuse components arise from light scattered in the spectrograph, principally from the grating. In a filter radiometer, the haze and diffuse components would correspond to spectral out-of-band features while the

specular component (the properly imaged radiation), would correspond to the in-band component.

Measurement errors arising from stray light are systematic errors with a magnitude that depends on the spectral distribution of the source being measured. Uncorrected, the scattered light in the MOS sensor illustrated in Fig. 10 causes unknown errors in the measured up-welling radiance. For a primary vicarious calibration instrument such as MOBY, these errors are potentially significant because they will not average out with repeat measurements and can lead to a bias in the calibration of satellite ocean color sensors. As we will show in Section 6, if not properly accounted for, this small fraction of scattered incident radiation in the MOS sensors would have a significant effect on ocean color research (Clark et al. 2002).

In Section 2, we describe an algorithm that corrects an instrument's response for stray or scattered radiation based on the characterization of its scattering properties. It is fundamentally a one-dimensional point-spread correction algorithm. In Section 3, the characterization of one of the MOS systems is described in detail. An uncertainty analysis of the stray light correction algorithm and validation measurements are described in Sections 4 and 5, respectively. In Section 6, we discuss the impact of the stray light correction of the MOS sensors on the calibration of MODIS and on satellite-based ocean color data products.

2. Stray Light Correction Algorithm

A number of algorithms have been developed to correct an instrument's imaging characteristics, in both one and two dimensions. One-dimensional algorithms generally correct an instrument's spectral response for scattered light; they are loosely referred to

as spectral stray light correction algorithms (Kostkowski 1997). In two dimensions, the algorithms are typically used to correct the spatial imaging of instruments such as the Hubble Space Telescope and are referred to as spatial stray light or point-spread response correction algorithms (Keel 1991; Jefferies and Christou 1993). To correct for image blurring in two dimensions, a point spread function (PSF) can be characterized and deconvoluted from the acquired image. In laboratory experiments, the PSF can be determined by imaging a point-source object such as a laser beam (Du and Voss, 2004), or by varying the position the spectrograph's entrance slit (Meister et al. 2005), or can be modeled from the measured bidirectional scatter distribution function, BSDF, of an instrument's optical elements (Qiu et al. 2000). In the field, a PSF can be developed by imaging a known object, such as the moon (Akira and Oyama 2005). PSFs for spectral stray light have been developed by scanning filters of know transmission (Kohler et al. 2004) or a source of known shape and color (Bitlis et al. 2007). In these previously developed approaches, an approximate *true* image is deconvolved from the detected signal and the PSF by Fourier transform or matrix inversion techniques or by iterative algorithms. The algorithms developed for correcting the MOS sensor response, both an iterative correction algorithm (Brown et al. 2003) and a matrix-based algorithm (Zong et al. 2006), correct an image for the small amount of improperly imaged, or scattered, light within the instrument's field-of-view. It is a subtle distinction that has important implications for the stability and robustness of the algorithms.

For MOS, any spatial information of the sources being measured within its field-of-view is ignored. That is, MOS averages the spatial dimension of the spectral radiance being measured, either a calibration source or up-welling radiance in the ocean. In this

case, the output of the spectrograph, which uses a two dimensional array detector, is integrated along a column, giving a one-dimensional response. A one-dimensional spectral stray light response correction algorithm is used to correct MOS for scattered light.

2.1. Stray light characterization: Development of the Stray-light Distribution Function (SDF) matrix

An instrument's system-level response can be characterized at a particular wavelength by measuring a monochromatic spectral line source. It is critical that the source does not have any emission other than the spectral line itself. In general, lasers fulfill this requirement, for example the laser line measurement shown in Fig. 10. For proper system-level instrument characterization, it is important that the instrument's entrance pupil be uniformly illuminated. For the MOS characterization, tunable lasers were introduced into an integrating sphere and MOS measured the radiance of the sphere at its exit port.

A spectral Line Spread Function (LSF) is used to describe a spectrograph's relative response to a fixed monochromatic excitation. It is the one-dimensional analog to the point spread function used to describe the two-dimensional spatial imaging characteristics of an instrument. The LSF for monochromatic radiation centrally imaged on array element j, is denoted $f_{\mathrm{LSF}\,i,\,j}$. The index j is fixed, dependent on the wavelength of the incident radiation; index i runs over all indices in the detector array. For a 512-element detector array like those used in MOS, i takes on the discrete values from 1 to

512. Figure 10 is an LSF, $f_{\mathrm{LSF}\,i,\,140}$ of MOS205, normalized by its peak value for convenience.

The sharp image peak highlighted in Fig. 10 is referred as the in-band region, and corresponds to the instruments bandpass, analogous to the "in-band" component of a filter radiometer's responsivity. Dividing the LSF by the in-band area and setting the pixels within the in-band area equal to zero gives the relative fractional amount of radiation incident on pixel *j* that is scattered on to other elements in the detector array. This relative fractional scattering function is known as the Stray-light Distribution Function, SDF, denoted $d_{i,j}$, and is shown in Fig. 11 for the LSF given in Fig. 10. The in-band area is approximated by summing the values of the defined in-band elements in the array. For MOS, there is a clear plateau region in the logarithmic LSF – seen at approximately 0.2 % of the maximum signal in Fig. 10. This level defines the separation between the in-band and the out-of-band, or scattered light, regions of the image.

To fully characterize an instrument's response for spectral stray light, the relative stray light response for every excitation array element *j* should be known. By tuning the incident laser such that scattering functions can be derived that cover the detector array, an SDF can be developed that describe the full scattering properties of the spectrograph *for incident radiation that falls on the CCD*. Incident radiation that does not fall on the CCD, so-called off-CCD radiation, is a separate issue and cannot be accounted for by this algorithm. For optimal results using this algorithm, off-CCD radiation should be eliminated through the use of band-pass filters, e.g. short-pass or long-pass filters.

In general, the SDF's of a spectrograph are wavelength dependent; that is, $d_{i,j}$ varies with the excitation element *j* as well as the detection element *i*. It is impractical to

directly measure the SDF for every element in the array (for MOS, for example, this would require 1024 laser line measurements, 512 measurements for each array). However, since the shape of $d_{i,j}$ typically changes smoothly across the array with excitation element j, the $f_{\mathrm{LSF}\,i,j}$ can be measured at intervals much larger than the detector element interval $(\Delta j >> 1)$, and the $d_{i,j}$ for j between the measured excitation elements can be obtained by interpolation.

With $d_{i,j}$ known for every excitation element j, the spectral scattering properties of the instrument can be fully characterized by a two dimensional, $n \times n$, Stray-light Distribution Function matrix (SDF matrix) $\vec{\vec{D}}$, where n is equal to the number of elements in the detector array. $\vec{\vec{D}}$ is formed by filling the columns of the matrix with the individual SDF's; that is, each column $j = J$ of the matrix $\vec{\vec{D}}$ is filled with a corresponding $d_{i,J}$ (i = 1 to n). Note that the diagonal elements of the matrix and surrounding elements within the instrument's bandpass are equal to 0 by definition.

$$\vec{\vec{D}} = \begin{bmatrix} d_{1,1} & d_{1,2} & \cdot & \cdot & d_{1,J} & \cdot & \cdot & d_{1,n-1} & d_{1,n} \\ d_{2,1} & d_{2,2} & \cdot & \cdot & d_{2,J} & \cdot & \cdot & d_{2,n-1} & d_{2,n} \\ \cdot & \cdot & \cdot & \cdot & \cdot & \cdot & \cdot & \cdot & \cdot \\ \cdot & \cdot & \cdot & \cdot & \cdot & \cdot & \cdot & \cdot & \cdot \\ d_{I,1} & d_{I,2} & \cdot & \cdot & d_{I,J} & \cdot & \cdot & d_{I,n-1} & d_{I,n} \\ \cdot & \cdot & \cdot & \cdot & \cdot & \cdot & \cdot & \cdot & \cdot \\ \cdot & \cdot & \cdot & \cdot & \cdot & \cdot & \cdot & \cdot & \cdot \\ d_{n-1,1} & d_{n-1,2} & \cdot & \cdot & d_{n-1,J} & \cdot & \cdot & d_{n-1,n-1} & d_{n-1,n} \\ d_{n,1} & d_{n,2} & \cdot & \cdot & d_{n,J} & \cdot & \cdot & d_{n,n-1} & d_{n,n} \end{bmatrix}, \qquad (1)$$

While each column j corresponds to the relative fractional amount of light hitting other array elements for a particular excitation wavelength, each row i in the matrix forms the relative *spectral* stray light response function for element $i=I$, $d_{I,j}$ (j = 1 to n).

That is, each row *i* in the matrix gives the relative amount of light scattered onto element *i* from all other elements *j* in the array. Knowing the amount of light falling on the other elements *j* of row *i*, where *j* is not equal to *i*, gives rise to the scattered light signal measured by detector element *i*. This is the crucial conceptual step in the algorithm. The total amount of scattered light falling on element *i* from all light incident on the detector, $y_{SL,i}$, can be expressed as:

$$y_{SL,i} = \sum_{j=1}^{n} \left(d_{ij} \cdot y_{IB,j} \right), \tag{2}$$

where $y_{IB,j}$ is the in-band signal from element *j* and the summation extends over all elements in the array.

2.2. The stray light correction algorithm

Consider the measurement equation for detector array element *i* for the case when a broad-band source is measured. The measured signal from element *i*, $y_{meas,i}$, is given by

$$y_{meas,i} = y_{IB,i} + y_{SL,i}^{total}, \tag{3}$$

where $y_{IB,i}$ is the measured in-band (IB) signal from element *i* and $y_{SL,i}^{total}$ is the total signal from element *i* arising from scattered light. $y_{SL,i}^{total}$ is the sum of all spectral stray light contributions from the broad-band source spectra falling on different elements in the array plus scattered light from all other sources, δ_i:

$$y_{SL,i}^{total} = \sum_{j=1}^{n} \left(d_{ij} \cdot y_{IB,j} \right) + \delta_i . \tag{4}$$

In particular, δ_i includes contributions from off-CCD scattered light. This is scattered light that is never imaged onto the detector array. There is a detected signal from this light because in most cases, the spectrum of a measured broad-band source extends beyond an instrument's designed spectral coverage range; in addition, the spectral response of the detectors used is typically broader than the designed spectral range. As previously stated, δ_i cannot be quantified and corrected with the algorithm being described; however, this component may be negligible or can be reduced to a negligible level by properly filtering the radiation entering the spectrograph.

In the MOS BSG, there is little UV energy in either calibration lamps or ocean water, and the dichroic mirror removes longer-wavelength red energy. For the MOS RSG, the long-pass filter removes shorter-wavelength energy, and the combined response of the CCD detector and its visible-band anti-reflection coating reduce response to IR wavelengths. Delta is therefore equal to zero in these systems. Setting δ_i equal to zero, Eq. 3 can be written as:

$$y_{meas,i} = y_{IB,i} + \sum_{j=1}^{n} \left(d_{ij} \cdot y_{IB,j} \right) \tag{5}$$

Considering all elements in the array, Eq. 5 can be expressed in matrix form,

$$\vec{Y}_{meas} = \vec{Y}_{IB} + \vec{\vec{D}} \cdot \vec{Y}_{IB}, \tag{6}$$

where $\vec{Y}_{meas}$ is a column vector comprised of the *n* measured signals from the detector array and $\vec{Y}_{IB}$ is a column vector representing the IB signals from the *n* array elements. Equation 6 can be rewritten as:

$$\vec{Y}_{meas} = \left[\vec{\vec{I}} + \vec{\vec{D}} \right] \cdot \vec{Y}_{IB} = \vec{\vec{A}} \cdot \vec{Y}_{IB} \quad , \tag{7}$$

where $\vec{\vec{A}} = \left(\vec{\vec{I}} + \vec{\vec{D}}\right)$ is a square coefficient matrix of order *n* and $\vec{\vec{I}}$ is the *n*×*n* identity matrix. $\vec{\vec{A}}$ has a particular form, with the in-band area of each element compressed into a single element along the matrix diagonal. The adjacent elements, those corresponding to the in-band area, are set equal to 0, and the other elements in the array are all much less than 1.

In Eq. 5, there are a total of *n* equations, and the *n* $y_{IB,i}$ are the unknown quantities of interest. The matrix measurement equation, Eq. 6, as well as Eq. 7, are systems of simultaneous linear equations that have the same number of equations as unknowns (*n*). Each unknown column vector $\vec{Y}_{IB}$ can be obtained by directly solving Eq. 7 using a proper linear algebraic algorithm (*e.g.* the Gaussian elimination algorithm). However, in terms of simplicity and calculation speed, it is preferable to solve Eq. 7 by inverting matrix $\vec{\vec{A}}$:

$$\vec{Y}_{IB} = \vec{\vec{A}}^{-1} \cdot \vec{Y}_{meas} = \vec{\vec{C}} \cdot \vec{Y}_{meas} . \tag{9}$$

$\vec{\vec{C}}$, the inverse of $\vec{\vec{A}}$, is called the spectral stray light correction matrix. Using Eq. 9, the spectral stray light correction becomes a single matrix multiplication operation, and the correction can be performed in real-time with minimal impact on acquisition speed. Note that development of matrix $\vec{\vec{C}}$, as with the development of matrix $\vec{\vec{D}}$, is required only once, unless the imaging or scattering characteristics of the instrument change.

3. Derivation of MOS Stray Light Correction Model Parameters

A total of 3 MOS systems have been characterized for 4 radiometric ocean color instruments. MOS202 is used in both the MOS Profiler and in the MOS ROV system; MOS204 is used in even-numbered MOBY buoy deployments; and MOS205 is the

sensor in odd-numbered MOBY buoy deployments. Because they have different input optics, the imaging is slightly different between the MOS Profiler and the MOS ROV systems. Therefore, $\vec{\vec{D}}$ matrices were independently developed for both systems, even though they used the same sensor. In the following discussion we will go through the development of the $\vec{\vec{D}}$ matrix in detail for the MOS ROV system.

The MOS ROV system was characterized on the NIST SIRCUS facility (Brown et al. 2000; Brown et al. 2006), using tunable lasers covering the entire MOS spectral range, from 350 nm to 960 nm. The lasers were introduced into a 30 cm diameter integrating sphere with a 7.5 cm diameter exit port. The MOS ROV fiber input was centered on the exit port, ensuring that the entrance pupil of the MOS system was over-filled. Representative laser line characterization data, normalized to a peak value of 1, and offset vertically for clarity of presentation, are shown in Fig. 12 for both ROV spectrographs. The in-band area is highlighted for each wavelength. A total of 80 laser lines were measured, ensuring adequate coverage to properly characterize rapidly changing features such as the spurious reflection peak highlighted by the arrows in the figure. For all MOS spectrographs the in-band limits were set at nine pixels to either side of the main peak. Only the relative spectral distribution as a function of array element is required for the stray light correction algorithm. The wavelength scale for each spectrograph is given on the top axis of each figure. Because of the 0.01 nm wavelength uncertainty on the SIRCUS facility, these data can be used to provide an accurate wavelength calibration of each spectrograph.

Normalizing the MOS ROV laser characterization data by the in-band area and setting the in-band pixels in each set of laser data to 0, the d_{ij} for j =100, 200, 300, 400,

and 500 are inserted as columns in a partial D-matrix shown in Fig. 13. The full matrices were formed by linearly interpolating the laser line data to fill in the intervening matrix elements. Figure 14 shows example rows, i = 100, 200, 300, 400 and 500 of the resulting D-matrix, while the full D-matrices for both spectrographs are shown in Fig. 15. The flat feature that can be seen in the first columns of the RSG D-matrix in Fig. 15b is due to the absence of laser lines there, and the result of linear interpolation from the first available laser line. Other attempted interpolation schemes produced undesirable effects when the stray light algorithm was applied.

The MOS systems used in MOBY were characterized in the buoy at the field calibration site in Honolulu, HI (Clark et al. 2003). Imaging for light entering the radiance port of each of the three arms was the same (Brown et al. 2003). Imaging remained constant for different even and odd buoy deployments, respectively. In fact, the imaging characteristics of the even buoy and odd buoy MOS systems have remained the same, within our ability to measure it, over the past 7 years. Consequently, only one SDF matrix was required for MOS204 and is applicable for the three radiance arms and all even buoy deployments. The same applies for MOS205 and odd buoy deployments.

Due to the fact that the MOBY sensors were characterized at the field site in Hawaii, only a subset of lasers was available. Continuous spectral coverage was available from 560 nm to 960 nm using a Ti:sapphire and a dye laser with DCM and Rhodamine 6G laser dyes. By intracavity doubling the Ti:sapphire laser, additional tunable coverage was available from 380 nm to 460 nm. For the spectral region between 460 nm and 560 nm, an argon-ion laser and a frequency-doubled Nd:Vanadate laser were used. These lasers emitted radiation at fixed frequencies, with the result that a total of ten

different wavelengths, or laser lines, were available for this critical spectral region. Instead of linearly interpolating the data between laser lines, the MOBY scattered light spectra were modeled and the modeled data were used to create the D matrices (Brown et al. 2003). In addition the reflection peak was very sharply distributed in the MOBY systems, being only a few pixels wide. In the modeled data, this width was compressed to a single pixel. Because the matrices were modeled using empirical fits to the laser line data, the uncertainties in the stray light correction algorithm will be higher for MOBY than for the MOS Profiler and MOS ROV systems.

Top view SDF matrices for the MOS ROV, both the red and the blue spectrographs, are shown in Fig. 16. The MOS Profiler matrices, although not shown here, have similar structure to that of the ROV, while the MOBY matrices' features are smoothed in comparison to the ROV, and the reflection peak appears sharper due to the fact that the matrix was modeled, not interpolated. In Figs. 15 and 16 there is a bright red line that crosses the main diagonal. This is the spurious reflection peak, highlighted by arrows in Fig. 12, which arises in the spectrographs from a mirror reflection coupled with a higher-order diffraction from the grating. As the laser image moves across the CCD array, the reflection peak changes size, shape, and position with respect to the primary peak.

4. Algorithm validation

To validate the stray light correction algorithm, a variety of colored sources are measured. One of the validation sources measured by the MOS ROV was a blue LED. The LED had a peak distribution at 450 nm and a FWHM bandwidth of 25 nm. It has no radiation to higher energy and very little radiation to lower energy outside of a 100 nm

window around the peak radiance. Fig. 17 shows the blue LED radiance measured by the ROV, uncorrected and corrected for stray light. There is no difference in the measured red spectrograph signal, uncorrected or corrected for stray light. No radiation was incident on that system. The stray light corrected spectrum for the blue spectrograph was approximately 2 orders of magnitude lower in the wings than the uncorrected spectrum. Because essentially any signal in the wings arises from scattered radiation, the figure shows the algorithm reduces the magnitude of the stray light signal in this measurement approximately 2 orders of magnitude.

5. Uncertainties

Measurement errors are inevitable, and arise from a variety of sources, including errors in coefficients $d_{i,j}$ due to errors in the LSFs (measured, interpolated, and modeled), errors in $\vec{Y}_{meas}$ arising from noise, and computational round-off errors. In order to obtain an accurate solution for $\vec{Y}_{IB}$ using Eq. 9, it is critical that the solution be numerically stable; that is, that the solution be insensitive to small errors in the coefficients of matrix $\vec{\vec{C}}$. Matrix $\vec{\vec{A}}$ is nearly the identity matrix: all diagonal components are unity with adjacent components all zero ($d_{i,j}$ equals zero inside the defined set of IB elements). The rest of the components in the matrix are typically three orders smaller than the diagonal elements (the values of $d_{i,j}$ are typically smaller than 10^{-3}). When $\vec{\vec{A}}$ is nearly the identity matrix, small errors in $\vec{\vec{D}}$, in $\vec{Y}_{meas}$, and in computational round-offs should only result in small errors in the solution, $\vec{Y}_{IB}$ (Moler 2004).

The numerical stability of a system of simultaneous linear equations can be evaluated mathematically by calculating the condition number, $k(\vec{\vec{A}})$, of its square

coefficient matrix $\vec{\vec{A}}$ (Moler 2004). The condition number is a relative error magnification factor of a system of simultaneous linear equations. Changes in either $\vec{Y}_{meas}$ or $\vec{\vec{A}}$ can cause changes $k(\vec{\vec{A}})$ times as large in the solution $\vec{Y}_{IB}$. The condition number of an identity matrix is 1, while the condition number of a singular square matrix is infinite. Table 1 shows the condition number calculated for the red and blue spectrographs for the different MOS configurations. Note that the condition number is close to 1 in all cases, implying that the matrix is numerically stable.

Because the $\vec{\vec{D}}$ matrices were developed through models for the MOBY MOS systems, a Monte Carlo approach was used to estimate the uncertainties in the stray light correction factors for MOBY up-welling and water-leaving radiance measurements (Brown et al. 2003). Uncertainty bounds were placed on each of the elements used to develop the modeled scattered light spectra. Values for each component were randomly chosen and the full stray light correction algorithm - correcting both the responsivity and the in-water data - was run for a typical in-water spectrum. The sequence was repeated 100 times and mean stray light correction factors and uncertainties were calculated. The uncertainties in the stray-light corrected up-welling radiance measurements are shown in Fig. 18 for deployment 219. Even deployments gave similar results. These results represent an upper-bound on the uncertainty as the uncertainty in each fit component was doubled for the Monte Carlo simulation to account for possible additional uncertainties in the model parameters arising from changing environmental conditions and other unknown factors.

The MOBY MOS systems will be brought to NIST at an appropriate time, where the impact on the acquisition of the continuous data set of water-leaving radiance is

negligible. New $\ddot{D}$ and $\ddot{C}$ matrices will be created based on a full set of laser line characterization data. If the imaging characteristics in these MOS systems do not change, these new $\ddot{D}$ and $\ddot{C}$ matrices can be applied to the full data set. In this case, characterization of the spectrographs on SIRCUS will impact the penultimate MOBY uncertainty budget in the blue spectral region. The residual uncertainties due to stray light should be reduced by a factor of 2 or more over the current uncertainties.

6. Impact on the vicarious calibration of MODIS and derived bio-optical data products

MOBY is used to vicariously calibrate MODIS ocean color bands 8 through 13; the band-center wavelengths are listed in Table 2. Since blue-band L_w contributes at most 10 % of the total radiance measured by a satellite sensor over clear ocean water, to achieve the goal of 5 % uncertainty in L_w, the satellite radiance vicarious calibration uncertainty target is 0.5 %. By making repeated measurements over the MOBY site concurrent with MOBY measurements, the random components in a satellite sensor's vicarious calibration uncertainty budget can be reduced to a manageable level. For example, the vicarious calibration of SeaWiFS visible bands utilized 150 MOBY match-ups over nearly a decade to determine a multiplicative gain correction to top-of-atmosphere radiance (Franz et al. 2007). MOBY-derived corrections for SeaWiFS varied between +3.8 % at 412 nm, and -2.6 % at 670 nm, with the standard deviation of the multipliers at or below 1 % for all wavelengths. These 1 % standard deviations yielded standard errors of about 0.1 % for the average SeaWiFS vicarious calibration gains, which are well within the total on-orbit uncertainty budget target of 0.5 %.

However, systematic uncertainty components will not average out with repeat measurements; they can lead to a bias in the calibration of satellite ocean color sensors. Errors arising from stray light are systematic errors. Their magnitude can be assessed by comparing the ratios of stray light corrected to uncorrected $L_w(\lambda)$ measured by MOBY. These ratios, band-weighted to each of the MODIS bands, for deployment 3 through deployment 33, covering the years from 1997 to 2007, are shown in Fig. 19. Ratios are shown for even and odd deployments, or for MOS204 and MOS205 sensors, respectively. The stability of the ratio is representative of the stability of the imaging in the two sensors. The increase in the Band 8 ratio for deployments 6, 8, and 10 in 1998 and 1999 was due to the use of a different optical fiber during those deployments. For these three deployments, low hydroxyl (OH) optical fibers were used to couple the radiance heads to MOS, which transmitted less light than the other fibers in the blue spectral region. For these three deployments, then, the relative stray-light contribution to the total signal in the blue was larger than for other buoys, resulting in the larger Band 8 ratio for these buoys. The mean stray light corrected-to-uncorrected water-leaving radiance ratios are given in Table 3. They range from a maximum value of +9.7 % for Band 8 (411.8 nm) to -4.3 % for Band 12 (546.8 nm).

Uncertainty in MOBY up-welling radiance measurements can be grouped into 4 categories: uncertainty in radiometric calibration sources, uncertainty in the transfer of radiometric scales to MOBY, the radiometric stability of MOBY during deployment, and environmental uncertainties during a MOBY deployment (Brown et al. 2007). Stray light in the MOS spectrographs, either uncorrected or corrected for, affects the uncertainty in transferring radiance scales from calibration standards to MOBY L_u and L_w. The

combined standard uncertainties for Top arm L_u under optimal environmental conditions, from Brown et al. (2007), are shown in Table 4, for comparison with the uncertainty in Top L_u stray-light correction from Fig. 18, and the average L_w stray-light correction factors from Fig. 19, for MODIS bands 8 to 13. Estimated combined standard uncertainty in Top L_u is from 2 to 3 % (k = 1), which includes uncertainty for stray light correction of 0.1 to 0.7 %. If left uncorrected, stray light translates directly to an almost 10 % measurement error in L_w at 412 nm. A bias of this magnitude is significant compared to the overall MOBY uncertainty budget.

Satellite ocean color data products are related to water-leaving radiance through bio-optical algorithms. A bio-optical algorithm relating the logarithm of High Performance Liquid Chromatography (HPLC) measured total chlorophyll-*a* concentration to the logarithm of MODIS Band 9 to Band 12 ratio is shown in Fig. 20. The radiometric sensor calibration errors arising from stray light will propagate through to global assays of satellite ocean color data products such as phytoplankton chlorophyll-*a*. Uncorrected for stray light, the MODIS Band 9 to Band 12 ratio is approximately 8 % low. This is a systematic error in the calibration coefficients, and will remain constant, independent of the spectral distribution of the water-leaving radiance measured by the sensor. Applying this bias to the bio-optical algorithm shown in Fig. 20, the error in retrieved chlorophyll-*a* concentration as a function of the log of the Band 9 to Band 12 ratio is given in Table 5. Values range from -29 % in high chlorophyll waters to -11 % in moderate chlorophyll waters, to -31 % in low chlorophyll-*a*, open-ocean waters. The target uncertainty in measured chlorophyll-*a* concentrations in the open ocean is 35 %.

Uncorrected, the calibration error arising from stray light dominates the scientific uncertainty goals for chlorophyll-*a*.

Stray light, if present in the instrumentation, will also impact bio-optical algorithm development. The MOS 202 system, utilized in the MOS Profiler and the MOS ROV, was used in the development of a hyperspectral Ocean Color Data Base. The database is used to create bio-optical algorithms for MODIS. The magnitude of the stray light correction is dependent on the spectral composition of the water mass (concentration of phytoplankton chlorophyll-*a*). Figure 21 shows MOS 202 data, uncorrected (grey circles) and corrected (black circles) for stray light, for the Band 9 to Band 12 MODIS bio-optical algorithm. For water with low chlorophyll-*a* concentrations, the stray light correction increases the Band 9 to Band 12 ratio. For the highest chlorophyll-*a* concentration water, the stray light correction shifts the Band 9 to Band 12 ratio in the opposite direction, to higher ratios. The solid lines in the figure are polynomial fits to the two stray light corrected and uncorrected data sets. Table 6 lists the percent changes in the bio-optical algorithm due to stray light for different Band 9 to Band 12 ratios. Algorithm changes range from – 8 % in high chlorophyll water to +22 % in the lowest chlorophyll water. The results illustrate the need to evaluate stray light in hyperspectral systems (or spectral out-of-band light for filter radiometers) used to create ocean color bio-optical algorithms.

7. Discussion and Summary

With the maturation of hyperspectral imagers, increasingly strict requirements are being imposed on quantitative imaging applications. As the uncertainty requirements become more demanding, reduction or elimination of systematic errors arising from

improperly imaged light becomes increasingly important. Single-grating spectrographs, a common foundation for hyperspectral imagers, have scattered light. This scattered light can cause significant errors in measured light fields with spectral distributions that differ significantly from the spectral distribution of the calibration source. The one-dimensional point spread correction algorithm applied in this work corrects for improperly imaged spectral light. The algorithm reduces contributions to the net signal from scattered light, higher-order diffracted light, and fluorescence one to two orders of magnitude (Y. Zong, NIST, personal communication). Characterization of the MOS sensors and development of stray light correction matrices for these instruments revealed and resolved a significant bias in measurements of water-leaving radiance. Application of the algorithm impacted the vicarious calibration of two U. S. ocean color satellite sensors, SeaWiFS and MODIS, resulting in higher quality global ocean color data products from these sensors. The first reprocessing of the MOBY L_w time-series to include a stray-light correction was made available to NASA in mid 2002, and a second reprocessing was available in early 2005.

Extension to two dimensions will lead to a spatial point spread correction algorithm that will correct imagery within an instrument's field-of-view. This algorithm does not sharpen up imagery, but corrects an image for the small amount of improperly imaged, or scattered, light within the instrument's field-of-view. It is especially useful for scenes comprised of a combination of bright and dark targets, for example the common situation where ocean color sensors measure a scene with a cloud in part of the image. In this case, a small amount of scattered light from the bright target (a cloud) can introduce significant measurement errors in the dark region of the image (the ocean).

Development of a two-dimensional, spatial stray light correction algorithm will greatly reduce the magnitude of this class of imaging error. For example, Qiu et al. (2000) and Meister et al. (2005) demonstrated the potential for reduced radiance bias errors in high-contrast images by applying extended point spread corrections (512 x 512 pixel array) modeled for MODIS Terra and Aqua ocean color bands.

8. Acknowledgements

The authors would like to acknowledge support for this work from NASA under contract NNG04HK331 and NOAA under contracts NA05AANEG0199 and NA05AANEG0013. Dennis Clark (Marine Optical Consulting, Arnold, MD) is affiliated with Space Dynamics Laboratory as part of a Joint NIST/Utah State University Program in Optical Sensor Calibration. The authors acknowledge also the anonymous reviewers for their valuable suggestions in improving the manuscript.

9. References

Akira, I. and E. Oyama, 2005: Correction of Stray Light and Filter Scratch Blurring for ASTER Imagery. *IEEE Trans. Geosci. Remote Sens.*, **43**, 2763-2768.

Bitlis, B, P. A. Jansson, and J. P. Allebach, 2007: Parametric point spread function modeling and reduction of stray light effects in digital still cameras. *Proc. of SPIE-IS&T Electronic Imaging*, **6498**(64980V), 1-8.

Brown, S. W., G. P. Eppeldauer, and K. R. Lykke, 2000: NIST facility for Spectral Irradiance and Radiance Responsivity Calibrations with Uniform Sources. *Metrologia*, **37**, 579-582.

Brown, S. W., G. P. Eppeldauer, and K. R. Lykke, 2006: Facility for spectral irradiance and radiance responsivity calibrations using uniform sources. *Appl. Opt.*, **45**, 8218-8237.

Brown, S. W., B. C. Johnson, S. J. Flora, M. E. Feinholz, M. A. Yarbrough, R. A. Barnes, Y. S. Kim, K. R. Lykke, and D. K. Clark, 2003: Stray-light correction of the Marine Optical Buoy. *Ocean Optics Protocols for Satellite Ocean Color Sensor Validation, Revision 4, Volume 6*. J. L. Mueller, G. S. Fargion and C. R. McClain. Greenbelt, MD, NASA's Goddard Space Flight Center. NASA/TM-2003-211621, 87-124.

Brown, S. W., S. J. Flora, M.E. Feinholz, M. A. Yarbrough, T. Houlihan, D. Peters, Y. S. Kim, J. L. Mueller, B. C. Johnson, and D. K. Clark , 2007: The Marine Optical BuoY

(MOBY) Radiometric Calibration and Uncertainty Budget for Ocean Color Satellite Vicarious Calibration. *Proc. SPIE,* **6744**(67441M), 12 pp.

Clark, D. K., M. E. Feinholz, M. A. Yarbrough, B. C. Johnson, S. W. Brown, Y. S. Kim, and R. A. Barnes, 2002: An overview of the radiometric calibration of MOBY. *Proc. SPIE*, **4483**, 64-76.

Clark, D. K., M. A. Yarbrough, M. E. Feinholz, S. Flora, W. Broenkow, Y. S. Kim, B. C. Johnson, S. W. Brown, M. Yuen, J. L. Mueller, 2003: MOBY, a radiometric buoy for performance monitoring and vicarious calibration of satellite ocean color sensors: measurement and data analysis protocols. *Ocean Optics Protocols for Satellite Ocean Color Sensor Validation, Revision 4, Volume 6*. J. L. Mueller, G. S. Fargion and C. R. McClain. Greenbelt, MD, NASA Goddard Space Flight Center. NASA/TM-2003-211621, 3-34.

Du, H., and K. J. Voss, 2004: Effects of point-spread function on calibration and radiometric accuracy of CCD camera. *Appl. Opt.,* **43**, 665-670.

Flora, S. J., D. W. Peters, and W. W. Broenkow, 2000: Oceanographic Profiling Observations from the MOCE-5 Cruise: 1-21 October 1999. *Moss Landing Marine Laboratories Tech. Pub. 00-1*. Moss Landing, CA, Moss Landing Marine Laboratories, 123 pp.

Franz, B. A., S. W. Bailey, P. J. Werdell, and C. R. McClain, 2007: Sensor-independent approach to the vicarious calibration of satellite ocean color radiometry. *Appl. Opt.*, **46**, 5068-5082.

Gordon, H. R., 1987: Calibration requirements and methodology for remote sensors viewing the ocean in the visible. *Remote Sens. Environ.*, **22**, 103-126.

Gordon, H. R., 1998: In-orbit calibration strategy for ocean color sensors. *Remote Sens. Environ.*, **63**, 265-278.

Guenther, B., W. Barnes, E. Knight, J. Barker, J. Harnden, R. Weber, M. Roberto, G. Godden, H. Montgomery, and P. Abel, 1996: MODIS calibration: a brief review of the strategy for the at-launch calibration approach. *J. Atmos. Oceanic Technol.*, **13**(2), 274-285.

Hooker, S. B., C. R. McClain, and A. Holmes, 1993: Ocean color imaging: CZCS to SeaWiFS. *J. Mar. Technol. Soc.*, **27**(1), 3-15.

Jefferies, S. M. and J. C. Christou, 1993: Restoration of astronomical images by iterative blind deconvolution. *The Astrophysical Journal*, **415**, 862-874.

Johnson, B. C., E. A. Early, R. E. Eplee, R. A. Barnes, and R. T. Caffrey, 1999: The 1997 Prelaunch Radiometric Calibration of SeaWiFS. *The Fifth SeaWiFS Intercalibration Round-Robin Experiment (SIRREX-5)*, S. B. Hooker, and E. R. Firestone. Greenbelt, MD, NASA Goddard Space Flight Center. NASA/TM-1999-206892(7), 75 pp.

Keel, W. C., 1991: A simple, photometrically accurate algorithm for deconvolution of optical images. *Pub. Astronomical Soc. Pacific*, **103**, 723-729.

Kelley, E. F., G. R. Jones, and T. A. Germer, 1998: The three components of reflection. *Information Display*, **14**, 24-29.

Kohler, D. D. R., W. P. Bissett, R. G. Steward, and C. O. Davis, 2004: New Approach for the radiometric calibration of spectral imaging systems. *Opt. Express*, **12**, 2463-2477.

Kostkowski, H. J., 1997: Chapter 4: Spectral Scattering. *Reliable Spectroradiometry*. La Plata, MD, Spectroradiometry Consulting, 57-87.

Moler, C. B., 2004: Linear Equations. *Numerical Computing with MATLAB*. Philadelphia, PA, Society for Industrial and Applied Mathematics, 53-92.

Meister, G., B. Franz, K Turpie, and R. McClain, 2005: The MODIS Aqua Point-Spread Function for Ocean Color Bands. *9th Int. Symp. on Physical Measurements and Signatures in Remote Sensing, ISPRS WG VII/1*, Beijing, China, **36**(7/W20), 334-336.

Mueller, J. L. and R. Austin, 2002: Instrument performance specifications. *Ocean Optics Protocols for Satellite Ocean Color Sensor Validation, Revision 3, Volume 1*. J. L. Mueller and G. S. Fargion. Greenbelt, MD, NASA Goddard Space Flight Center. NASA/TM-2002-21004, 48-59.

O'Reilly, J. E., S. Maritorena, B. G. Mitchell, D. A. Siegel, K. L. Carder, S. A. Garver, M. Kahru, and C. McClain, 1998: Ocean color chlorophyll algorithms for SeaWiFS. *J. Geophys. Res.,* **103**(C11), 24937-24953.

Qiu, S., G. Godden, X. Wang, and B. Guenther, 2000: Satellite-Earth remote sensor scatter effects on Earth scene radiometric accuracy. *Metrologia,* **37**, 411-414.

Taylor B.N. and C.E. Kuyatt, 1994: Guidelines for Evaluating and Expressing the Uncertainty of NIST Measurement Results. *NIST Tech. Note,* 1297, 20 pp.

Yarbrough, M., M. Feinholz, S. Flora, T. Houlihan, B. C. Johnson, Y. S. Kim, M. Y. Murphey, M. Ondrusek, and D. K. Clark, 2007: Results in coastal waters with high resolution in situ spectral radiometry: The Marine Optical System ROV. *Proc. SPIE,* **6680**(66800I), 12 pp.

Zong, Y., S. W. Brown, B. C. Johnson, K. R. Lykke, and Y. Ohno, 2006: Simple spectral stray light correction method for array spectroradiometers. *Appl. Opt.,* **45**, 1111-1119.

Table Caption List

Table 1. Stray light matrix condition numbers calculated for the MOS systems.

Table 2. MODIS Terra band-center wavelengths.

Table 3. Average MODIS Terra band, stray light correction factors, L_w corrected / uncorrected, for even (MOS204) and odd (MOS205) buoy deployments.

Table 4. MOBY Top arm L_u uncertainty estimates and L_w correction factor.

Table 5. Percent change in MODIS-measured HPLC total chlorophyll-a due to the stray light correction of MOBY for different log Band 9 to Band 12 ratios.

Table 6. Percent change in the MODIS Band 9 to Band 12 ratio bio-optical algorithm due to the stray light correction of MOS202 (MOS Profiler and MOS ROV).

Figure Caption List

Figure 1. Schematic diagram of MOBY.

Figure 2. Schematic diagram of the MOS sensor optical layout. For the MOS systems that reside in the instrument bay in MOBY, an optical multiplexer replaces the single E_λ position.

Figure 3. Light fields measured by MOBY. (a) Down-welling surface irradiance (E_s); (b) Down-welling irradiance (E_d) measured by the Top arm, 1.5 m depth; (c) Down-welling irradiance measured by the Mid arm, 5 m depth; (d) Down-welling irradiance measured by the Bot arm, 9 m depth (e) Up-welling radiance (L_u)measured by the Top arm, 1.5 m depth; (f) Up-welling radiance measured by the Mid arm, 5 m depth; and (g) Up-welling radiance measured by the Bot arm, 9 m depth. Note that these data have been corrected for stray light.

Figure 4. (top) Schematic diagram of the MOS Profiler with the TET flotation rig. (bottom) The MOS Profiler on a ship's deck prior to deployment.

Figure 5. (top) Schematic diagram of the MOS ROV deployed from a ship. (bottom) The MOS ROV with fiber input port, irradiance collector, MOS system, and computer interface.

Figure 6. Representative up-welling radiance distributions from water with low phytoplankton chlorophyll-*a* concentration (blue water) and water with moderate phytoplankton chlorophyll-*a* concentration (green water) measured by the MOS Profiler during the Marine Optical Characterization Experiment-5 (MOCE-5).

Figure 7. Up-welling radiance distribution of high-chlorophyll, turbid water in the Chesapeake Bay and coral fluorescence in Kaneohe Bay, Hawaii measured by the MOS ROV.

Figure 8. (a) A typical up-welling spectral radiance measured by MOBY; (b) The spectral distribution of a lamp-illuminated integrating sphere source.

Figure 9. Up-welling radiance measured by (a) the Top, (b) the Mid and (c) the Bot MOBY arms, uncorrected for stray light.

Figure 10. Line spread function of MOS205, blue spectrograph, to monochromatic laser excitation centered at array element 140. The dark highlighted region corresponds to the in-band region of the image. Note that the vertical axis is scaled in "arbitrary units" (a.u.)

Figure 11. The Stray-Light Distribution Function, SDF, $d_{i,j}$ for the Line Spread Function, LSF, shown in Fig. 10.

Figure 12. ROV laser line characterization data for (a) the Blue Spectrograph and (b) the Red Spectrograph. The in-band region of each image is highlighted in black and arrows highlight spurious reflection peaks.

Figure 13. ROV d_{ij} for j=100, 200, 300, 400, and 500 for (a) the Blue Spectrograph and (b) the Red Spectrograph.

Figure 14. ROV partial D-matrix formed from the d_{ij} shown in Fig. 13 for (a) the Blue Spectrograph and (b) the Red Spectrograph.

Figure 15. ROV full D-matrix for (a) the Blue Spectrograph and (b) the Red Spectrograph. The center pixels have been given a nominal value of 1e-6 instead of 0 for these logarithmic graphs.

Figure 16. Top view of the D-matrix for (a) ROV, Blue Spectrograph; (b) ROV, Red Spectrograph.

Figure 17. (a) Uncorrected and (b) stray light corrected MOS ROV measurements of a blue LED diver lamp.

Figure 18. Results of Monte Carlo uncertainty analysis. Grey circles represent band-center wavelengths of MODIS Terra bands.

Figure 19. The ratio of stray light corrected over uncorrected water leaving radiance for MODIS Bands 8 through 13. Data show all deployments from September 1997 (deployment 3) through June 2007 (deployment 33). Data for even and odd buoys, MOS204 and MOS205, are shown.

Figure 20. MODIS Terra bio-optical algorithm relating the log of HPLC-measured total chlorophyll-*a* to the log of MODIS Band 9 to Band 12 water-leaving radiance ratio. The data are shown as solid circles; the solid line is a 5^{th} order polynomial fit to the data.

Figure 21. MODIS Band 9 to Band 12 water-leaving radiance data corrected (dark circles) and uncorrected (grey circles) for stray light. The dark and grey solid lines are 5^{th} order, polynomial fits to the data.

Table 1. Stray light matrix condition numbers calculated for the MOS systems.

	Blue Spectrograph	Red Spectrograph
MOS ROV	1.133	1.289
MOS Profiler	1.252	1.457
Even MOBY	1.302	1.095
Odd MOBY	1.224	1.226

Table 2. MODIS Terra band-center wavelengths.

MODIS Terra Band	Band-center Wavelength (nm)
8	411.8
9	442.1
10	486.9
11	529.7
12	546.8
13	665.6

Table 3. Average MODIS Terra band, stray light correction factors, L_w corrected / uncorrected, for even (MOS204) and odd (MOS205) buoy deployments.

MODIS Band	Even Buoy (MOS204)	Odd Buoy (MOS205)
8	1.095	1.097
9	1.033	1.039
10	1.012	1.015
11	0.962	0.964
12	0.962	0.957
13	1.007	1.044

Table 4. MOBY Top arm L_u uncertainty estimates and L_w correction factor.

MODIS Band	LuTop Combined Standard Unc. (%)	LuTop SLC Uncertainty (%)	Average Lw Correction Factor (%)
8	2.4	0.66	+ 9.6
9	2.1	0.29	+ 3.6
10	2.4	0.13	+ 1.4
11	2.3	0.21	- 3.7
12	2.4	0.36	- 4.0
13	3.3	0.64	+ 2.3

Table 5. Percent change in MODIS-measured HPLC total chlorophyll-a due to the stray light correction of MOBY for different log Band 9 to Band 12 ratios.

Log MODIS (Band 9/Band 12)	Change in HPLC total chlorophyll-a (%)
-0.600	-28.8
-0.400	-19.7
-0.200	-14.5
0.000	-11.0
0.200	-8.4
0.400	-6.8
0.600	-8.2
0.800	-15.7
1.000	-31.8

Table 6. Percent change in the MODIS Band 9 to Band 12 ratio bio-optical algorithm due to the stray light correction of MOS202 (MOS Profiler and MOS ROV).

Log MODIS (Band 9/Band 12)	Change in HPLC total chlorophyll-a (%)
-0.6000	-7.8
-0.4000	-1.8
-0.2000	7.3
0.0000	9.6
0.2000	6.5
0.4000	5.0
0.6000	10.8
0.8000	22.6
1.0000	21.6

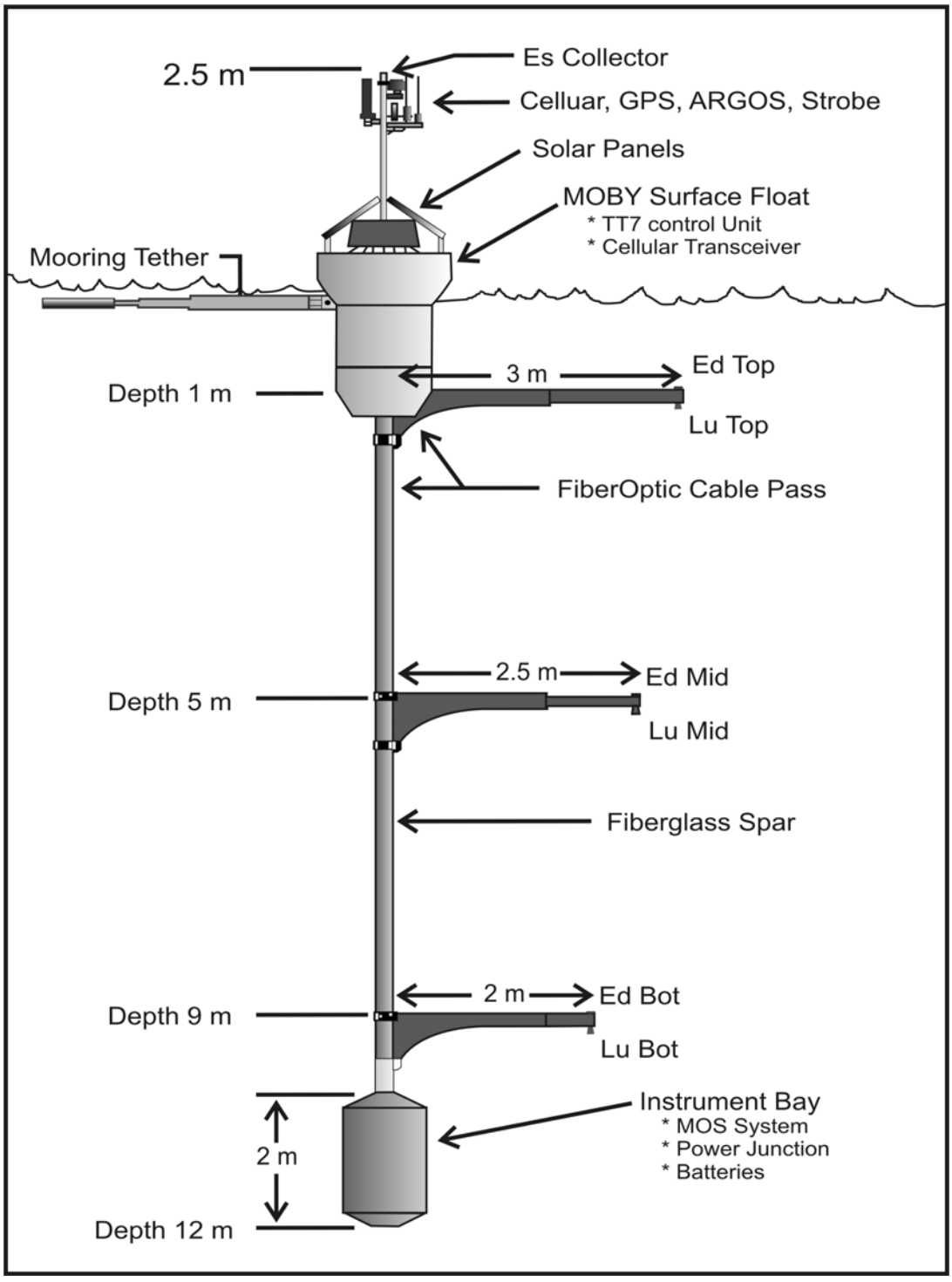

Figure 1. Schematic diagram of MOBY.

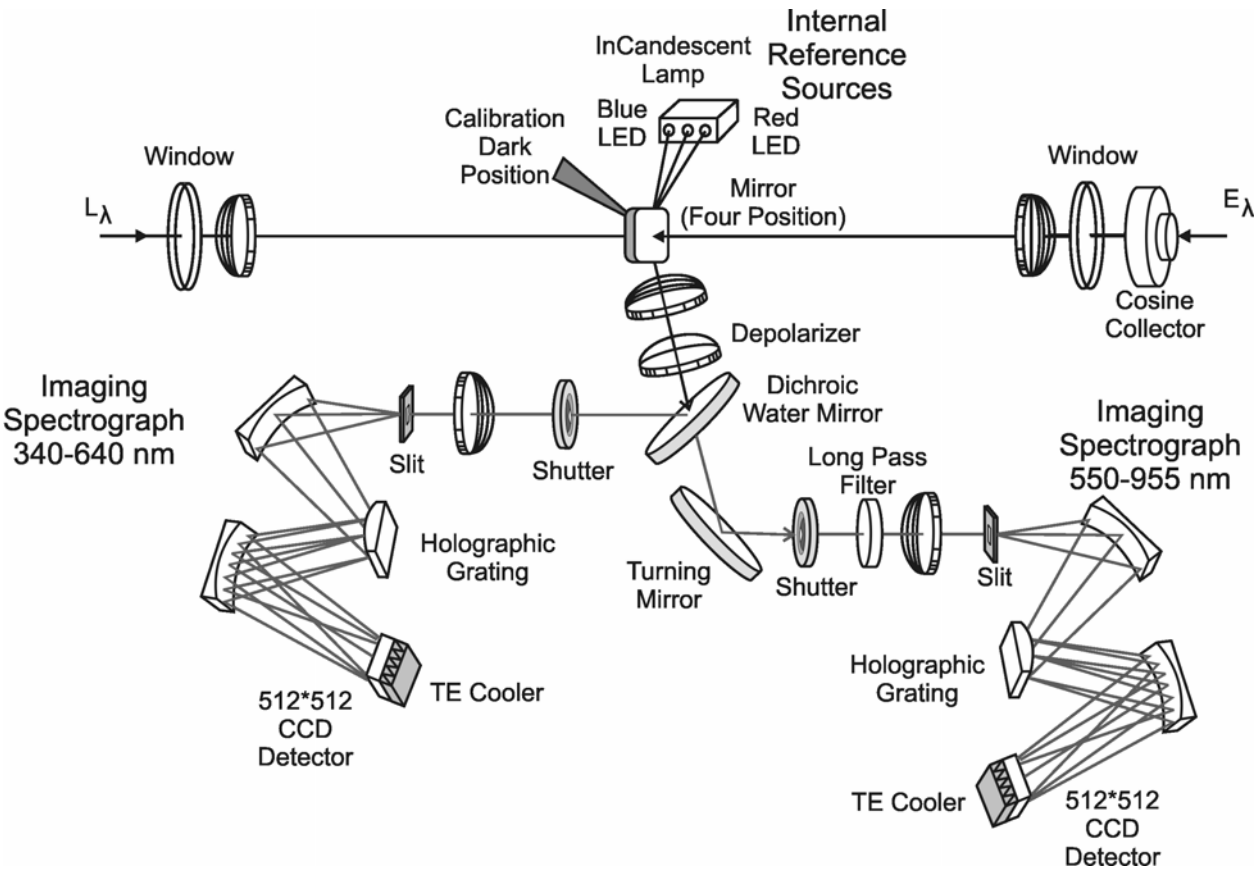

Figure 2. Schematic diagram of the MOS sensor optical layout. For the MOS systems that reside in the instrument bay in MOBY, an optical multiplexer replaces the single E_λ position.

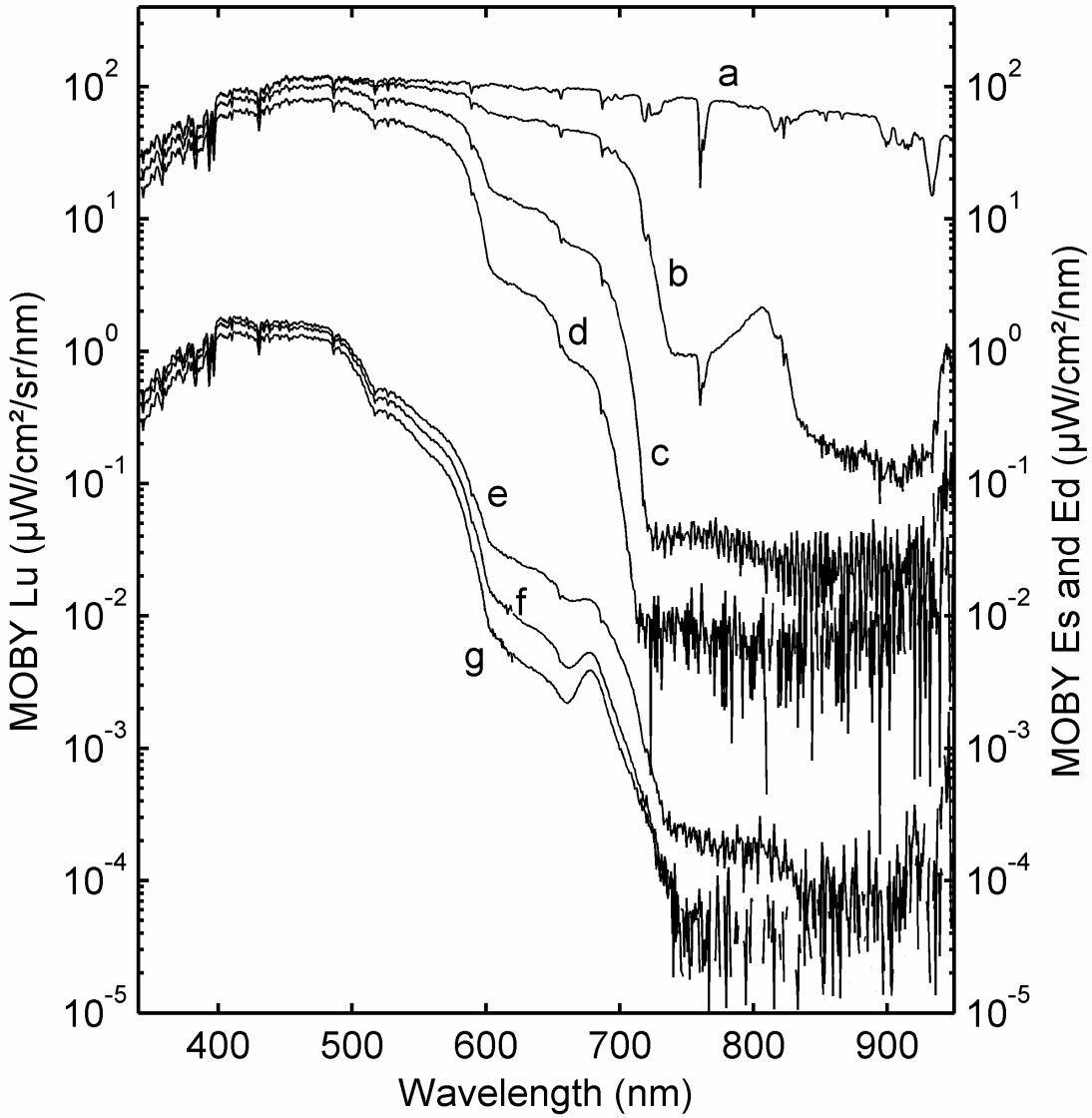

Figure 3. Light fields measured by MOBY. (a) Down-welling surface irradiance (E_s); (b) Down-welling irradiance (E_d) measured by the Top arm, 1.5 m depth; (c) Down-welling irradiance measured by the Mid arm, 5 m depth; (d) Down-welling irradiance measured by the Bot arm, 9 m depth (e) Up-welling radiance (L_u)measured by the Top arm, 1.5 m depth; (f) Up-welling radiance measured by the Mid arm, 5 m depth; and (g) Up-welling radiance measured by the Bot arm, 9 m depth. Note that these data have been corrected for stray light.

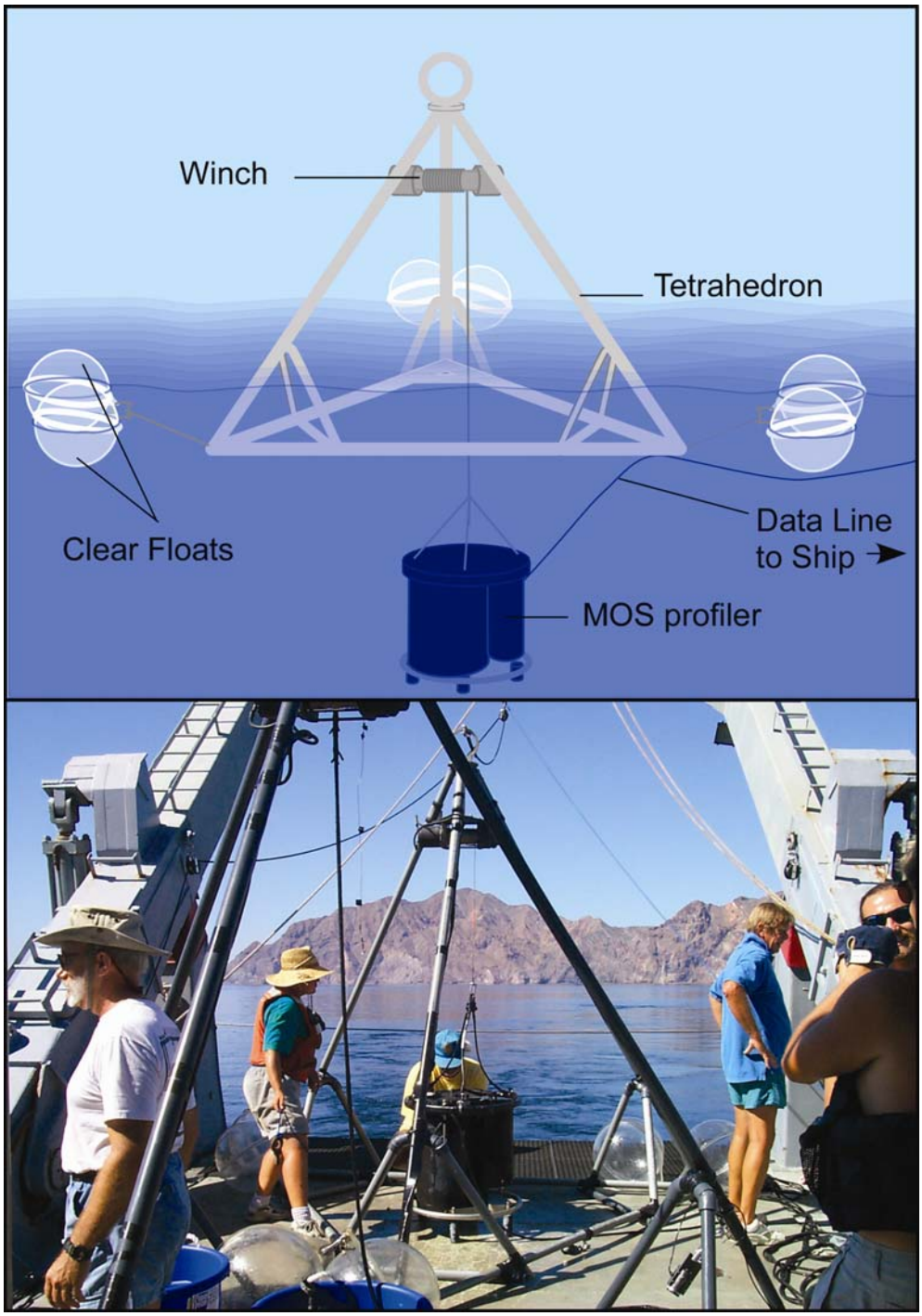

Figure 4. (top) Schematic diagram of the MOS Profiler with the TET flotation rig. (bottom) The MOS Profiler on a ship's deck prior to deployment.

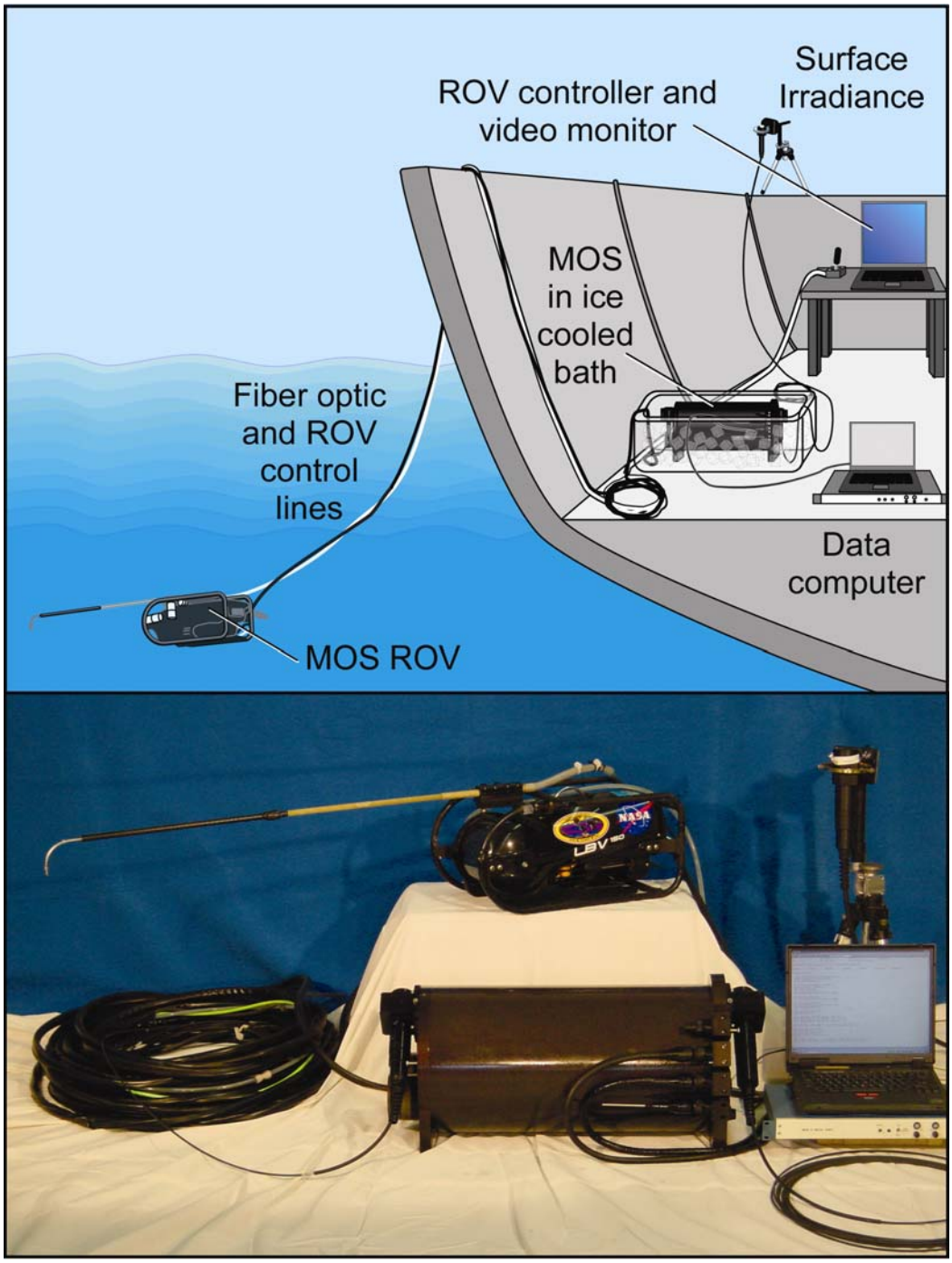

Figure 5. (top) Schematic diagram of the MOS ROV deployed from a ship. (bottom) The MOS ROV with fiber input port, irradiance collector, MOS system, and computer interface.

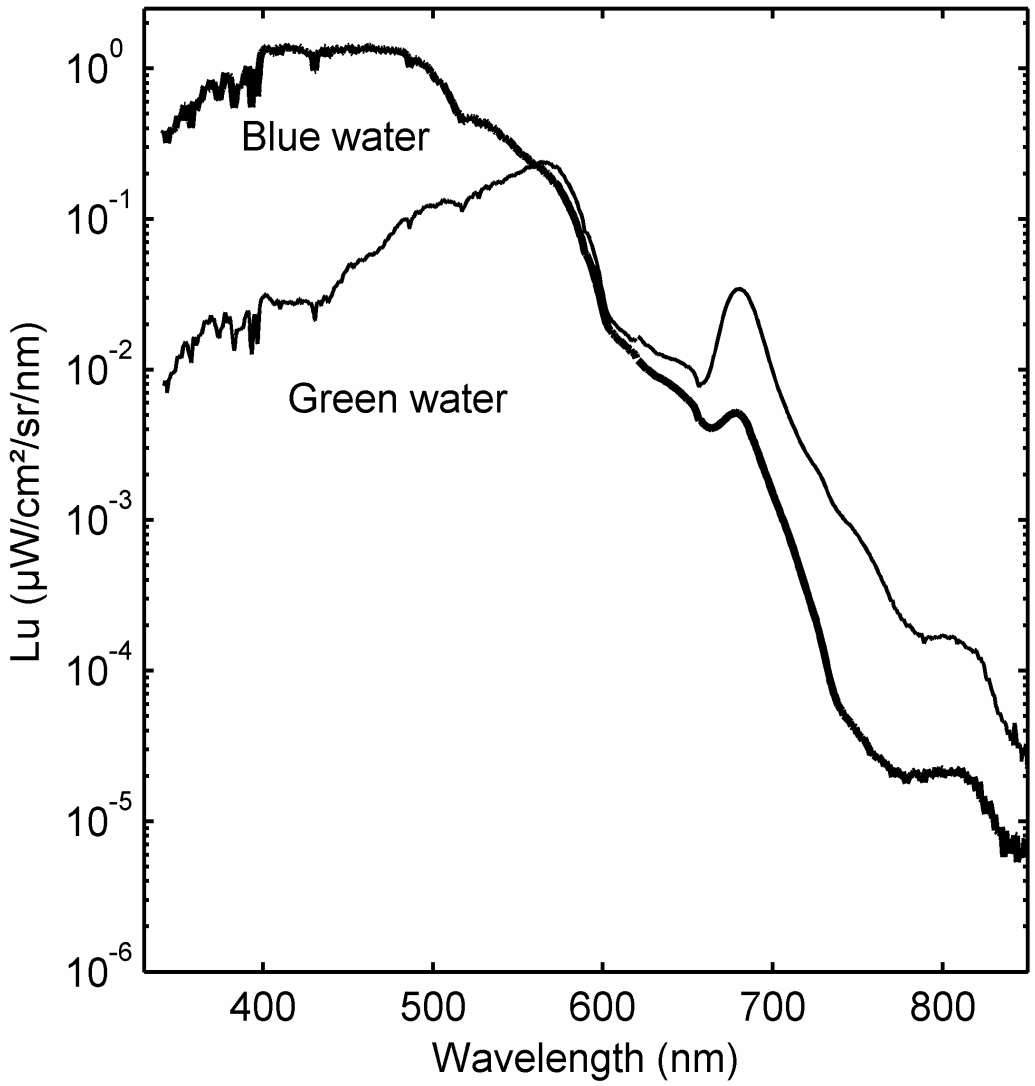

Figure 6. Representative up-welling radiance distributions from water with low phytoplankton chlorophyll-*a* concentration (blue water) and water with moderate phytoplankton chlorophyll-*a* concentration (green water) measured by the MOS Profiler during the Marine Optical Characterization Experiment-5 (MOCE-5).

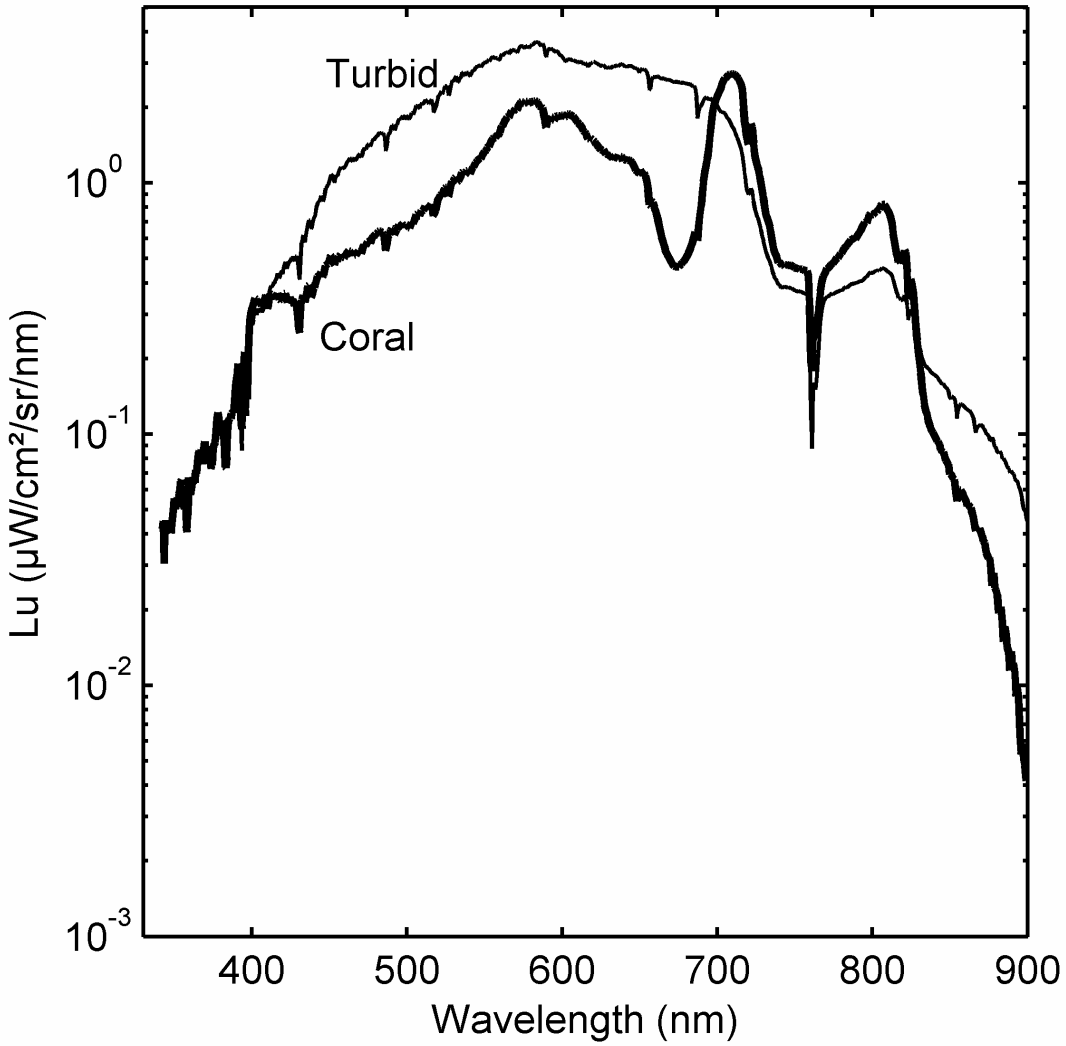

Figure 7. Up-welling radiance distribution of high-chlorophyll, turbid water in the Chesapeake Bay and coral fluorescence in Kaneohe Bay, Hawaii measured by the MOS ROV.

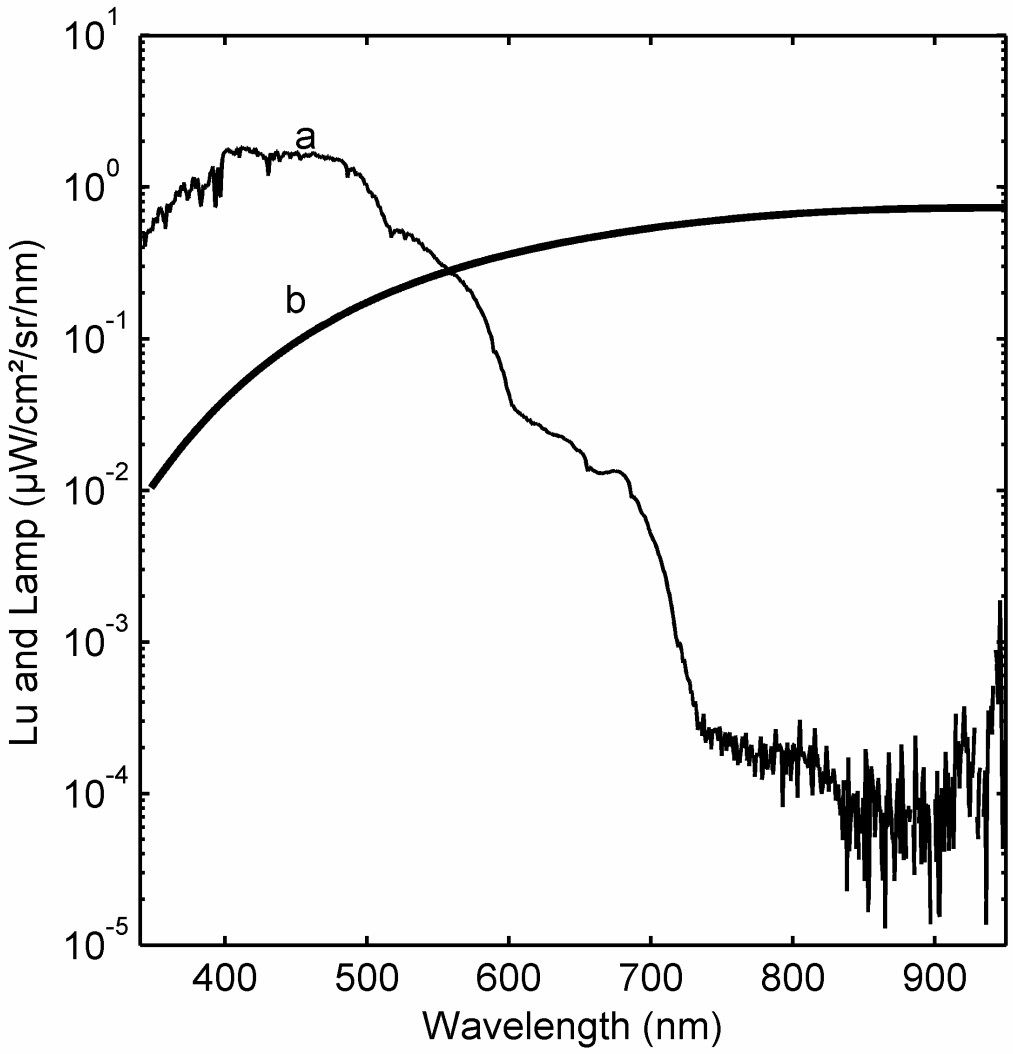

Figure 8. (a) A typical up-welling spectral radiance measured by MOBY; (b) The spectral distribution of a lamp-illuminated integrating sphere source.

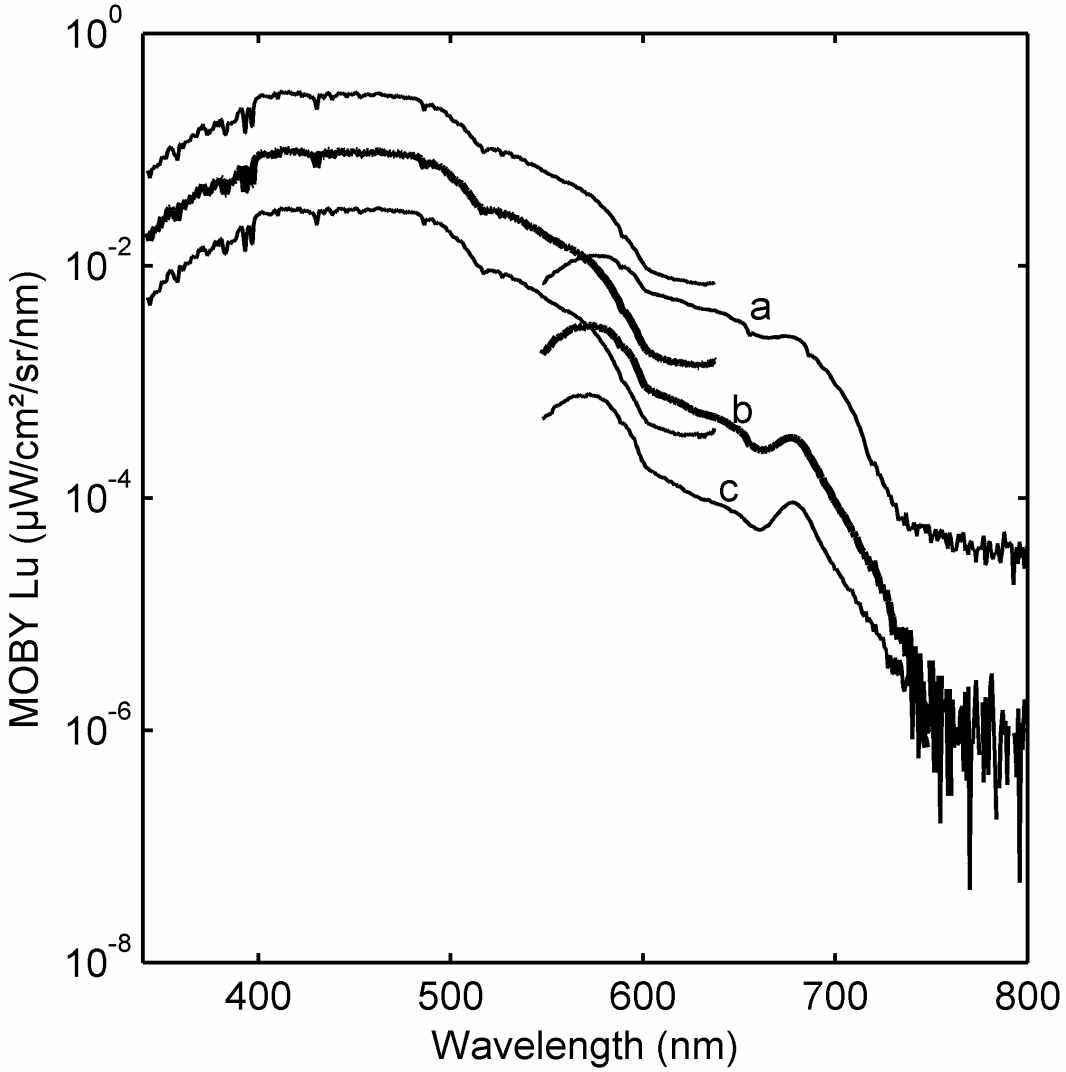

Figure 9. Up-welling radiance measured by (a) the Top, (b) the Mid and (c) the Bot MOBY arms, uncorrected for stray light.

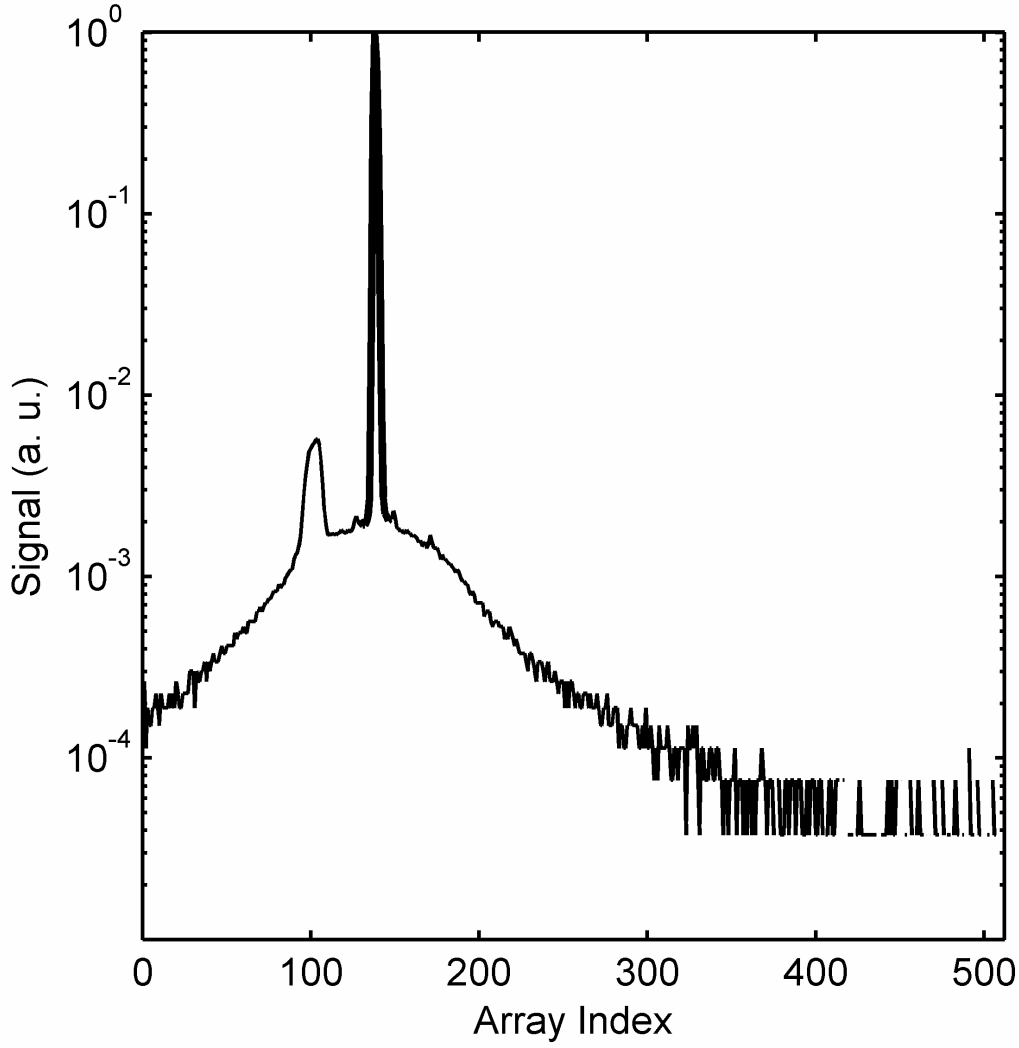

Figure 10. Line spread function of MOS205, blue spectrograph, to monochromatic laser excitation centered at array element 140. The dark highlighted region corresponds to the in-band region of the image. Note that the vertical axis is scaled in "arbitrary units" (a.u.)

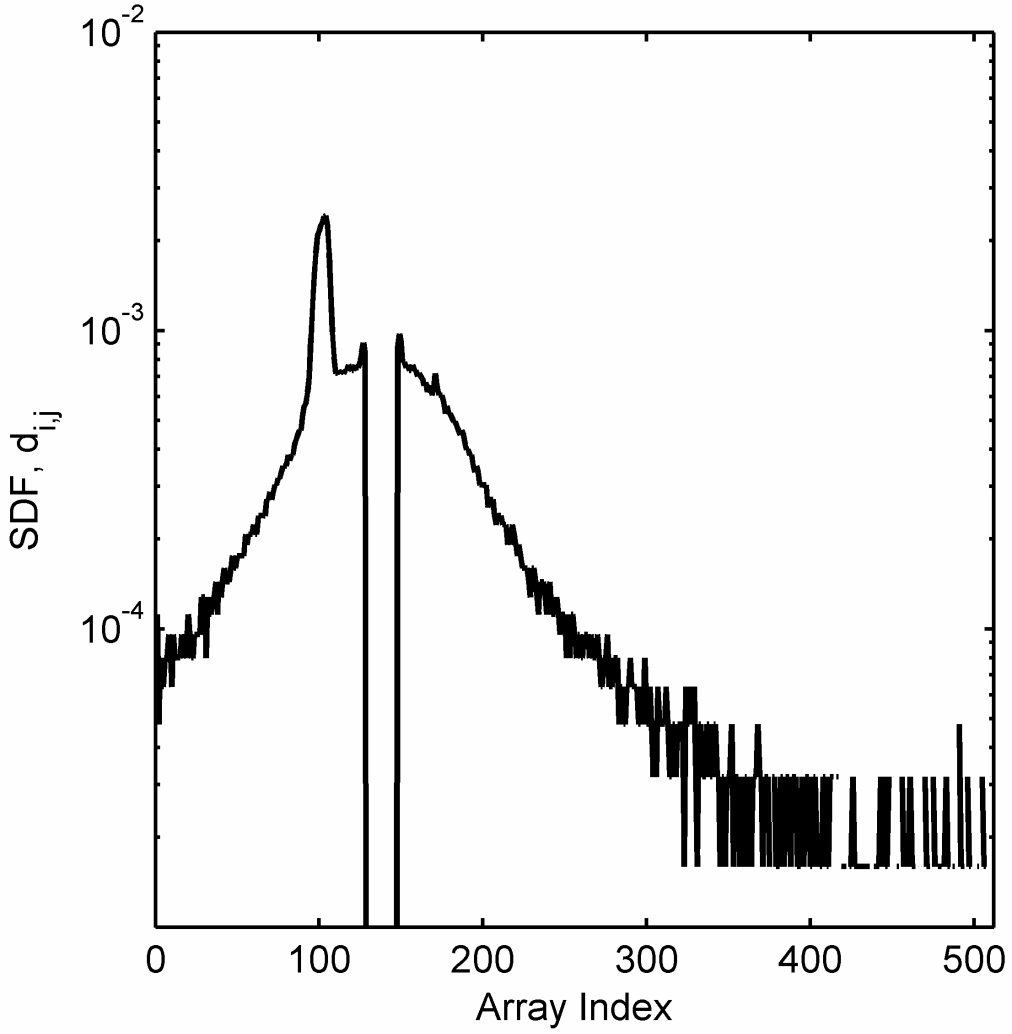

Figure 11. The Stray-Light Distribution Function, SDF, $d_{i,j}$ for the Line Spread Function, LSF, shown in Fig. 10.

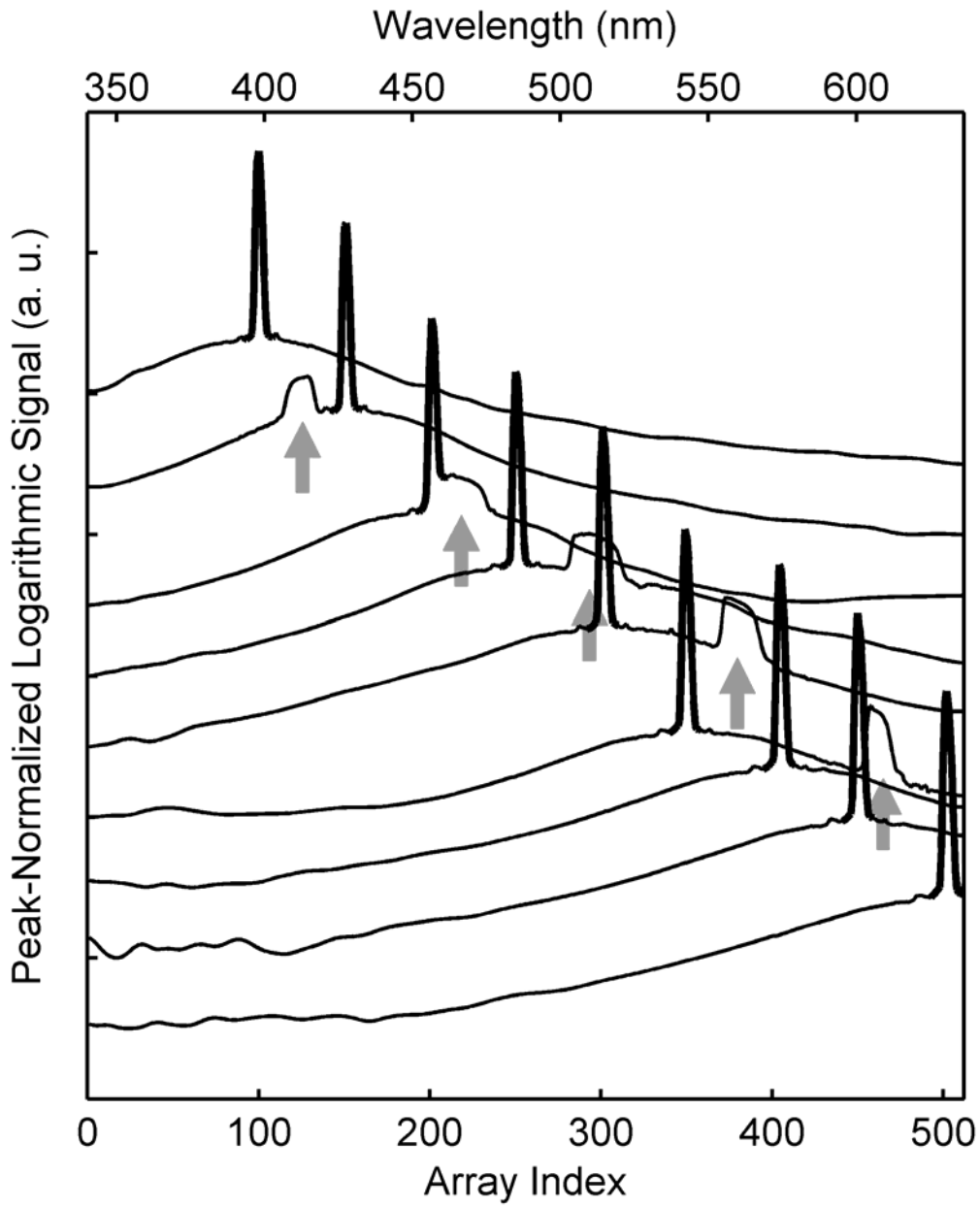

Figure 12(a). ROV laser line characterization data for the Blue Spectrograph. The in-band region of each image is highlighted in black.

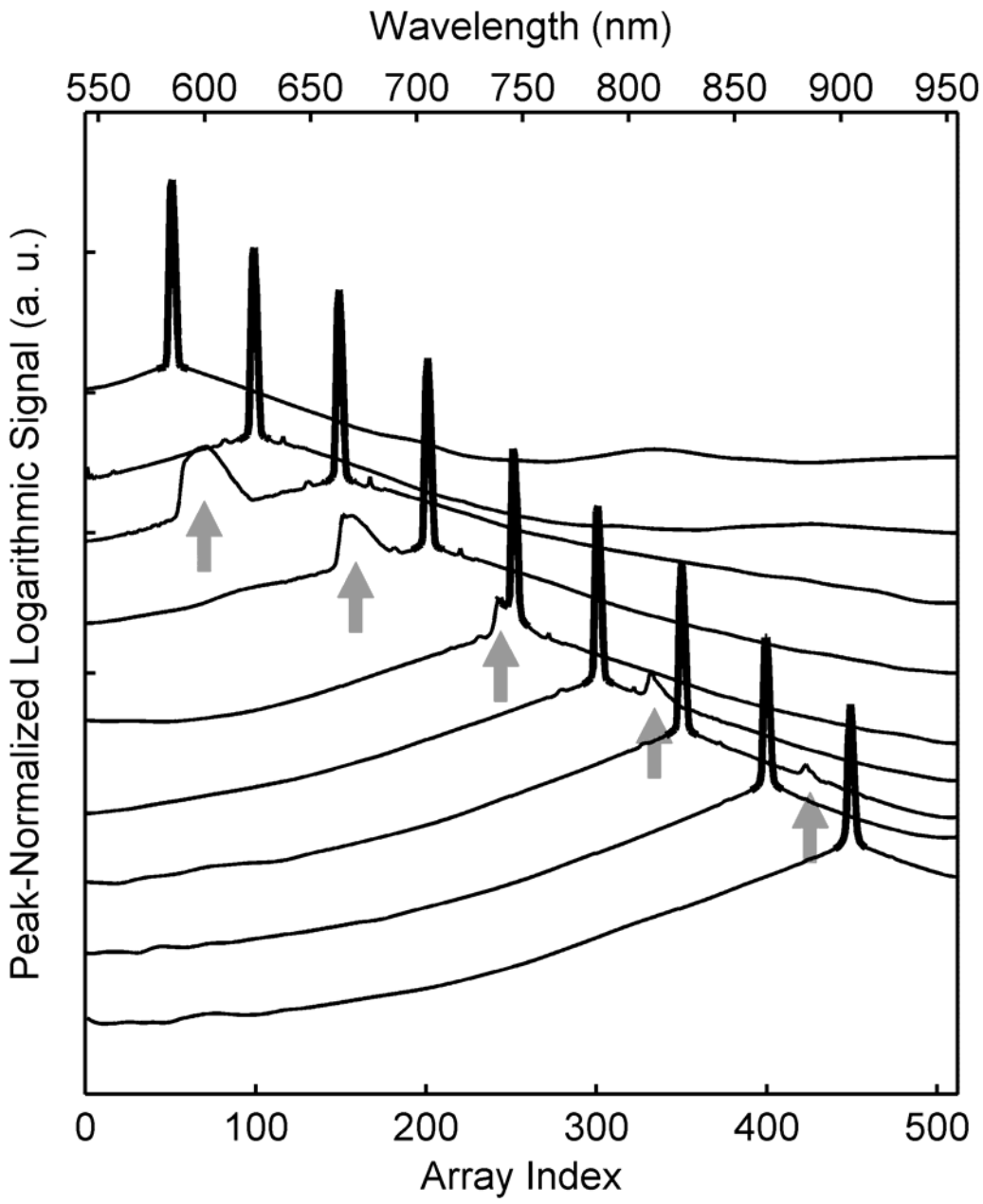

Figure 12(b). ROV laser line characterization data for the Red Spectrograph. The in-band region of each image is highlighted in black.

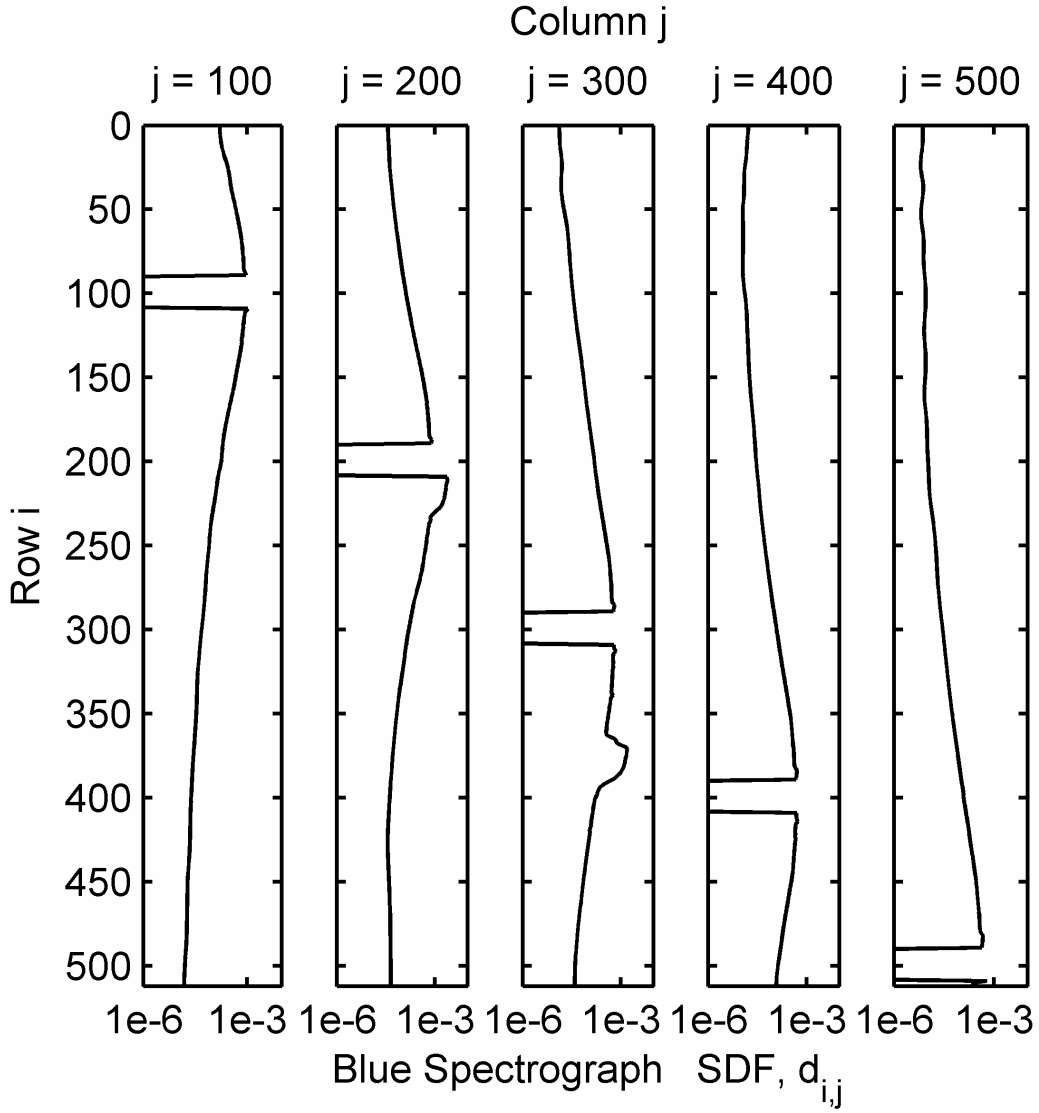

Figure 13(a). ROV d_{ij} for j=100, 200, 300, 400, and 500 for the Blue Spectrograph.

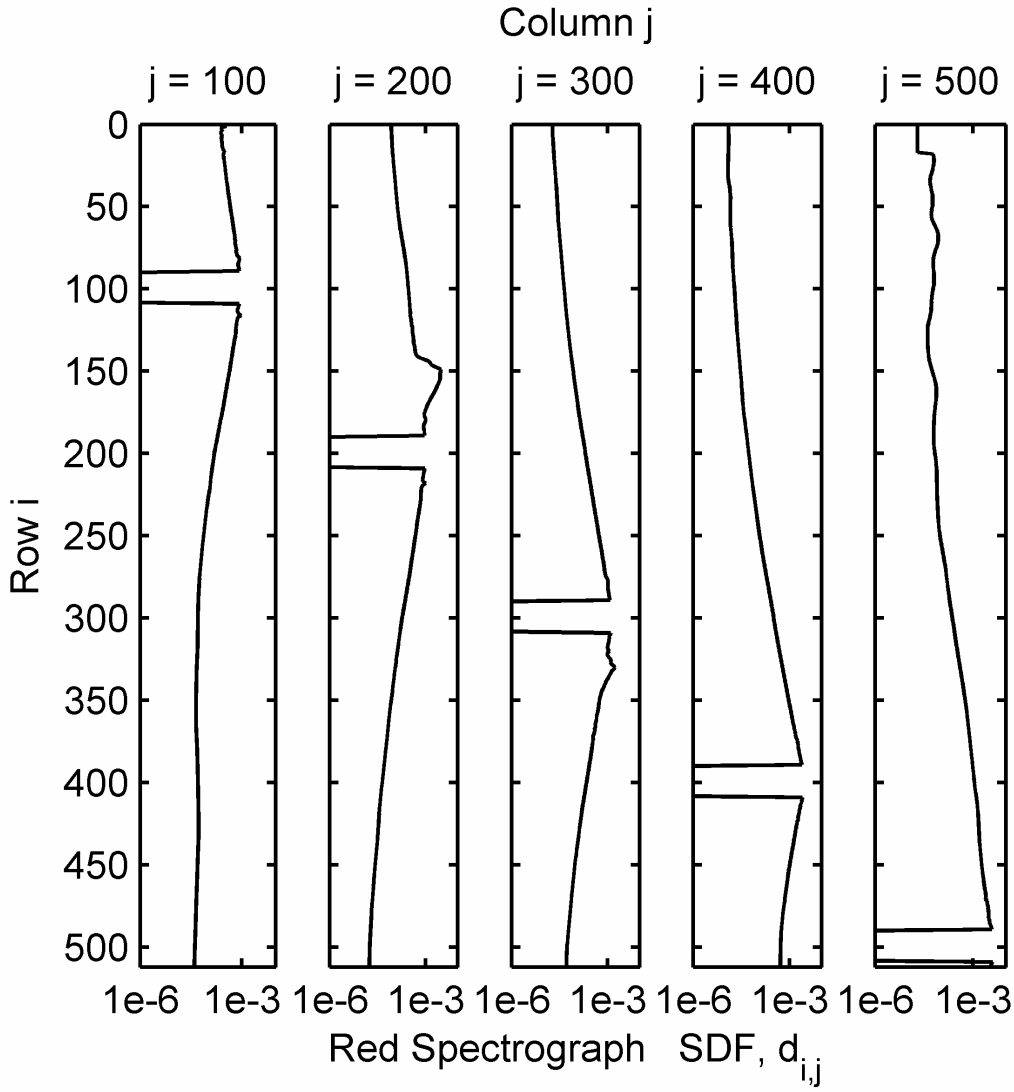

Figure 13(b). ROV d_{ij} for j=100, 200, 300, 400, and 500 for the Red Spectrograph.

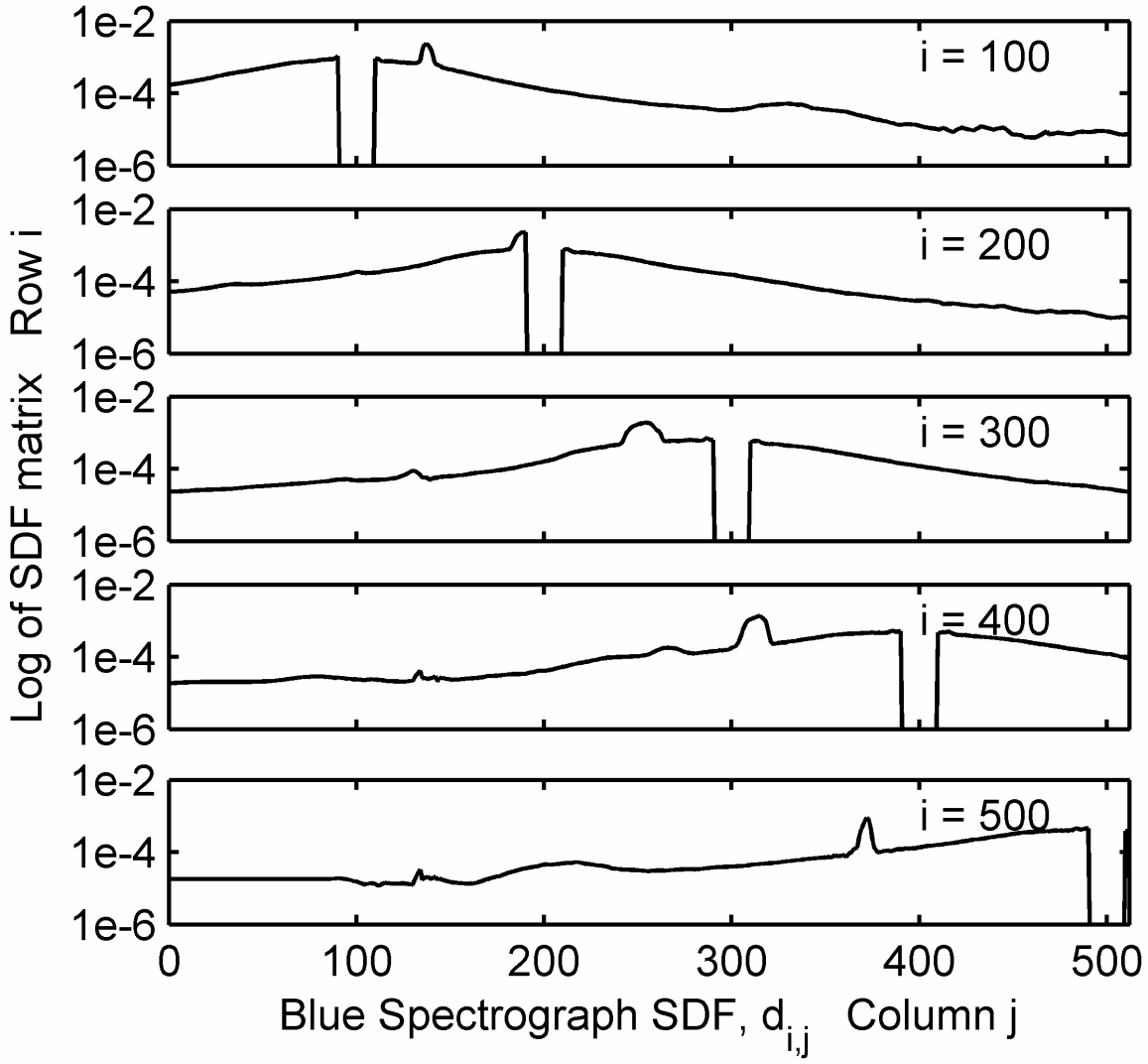

Figure 14(a). ROV partial D-matrix formed from the d_{ij} shown in Fig. 13 for the Blue Spectrograph.

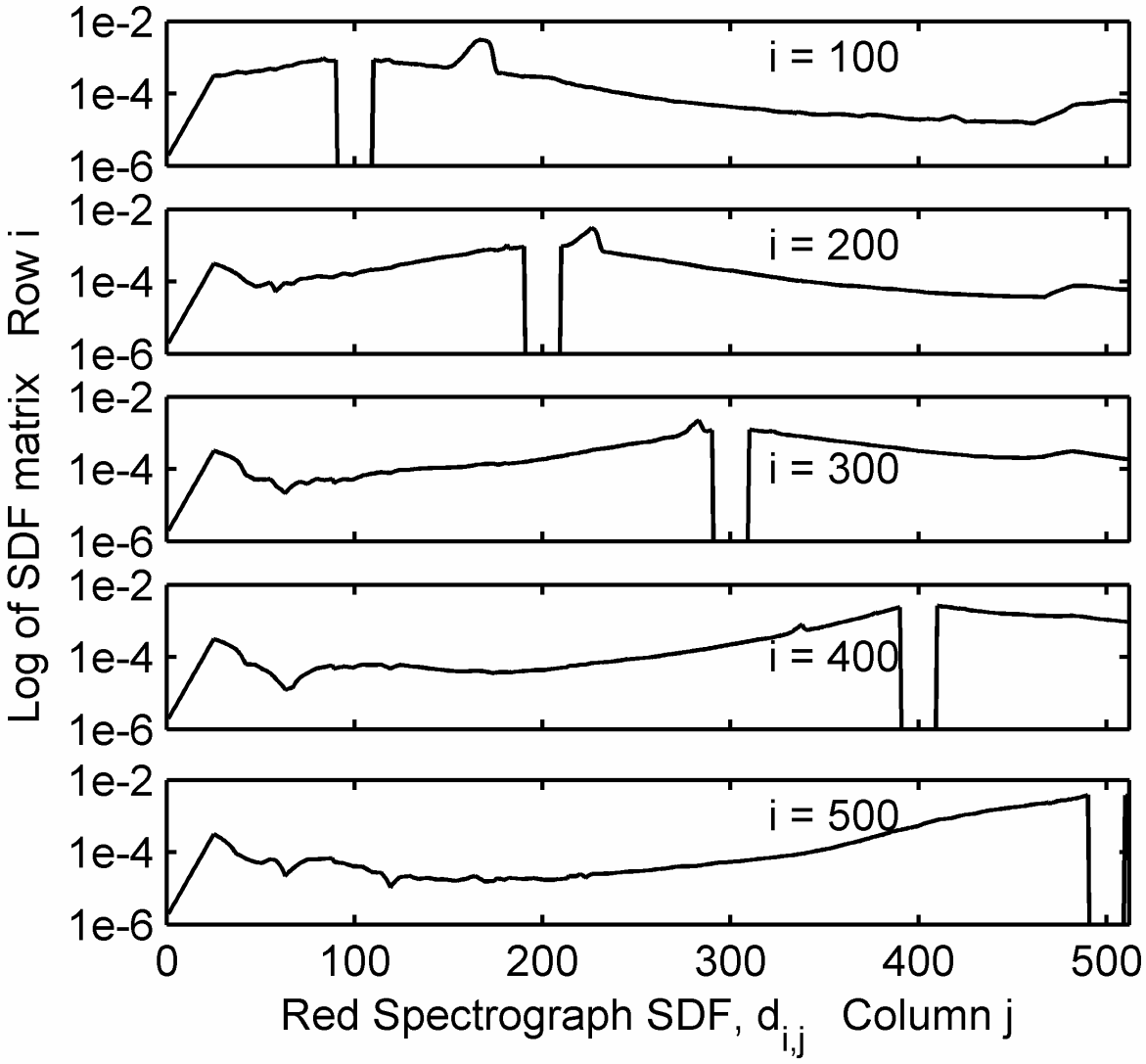

Figure 14(b). ROV partial D-matrix formed from the d_{ij} shown in Fig. 13 for the the Red Spectrograph.

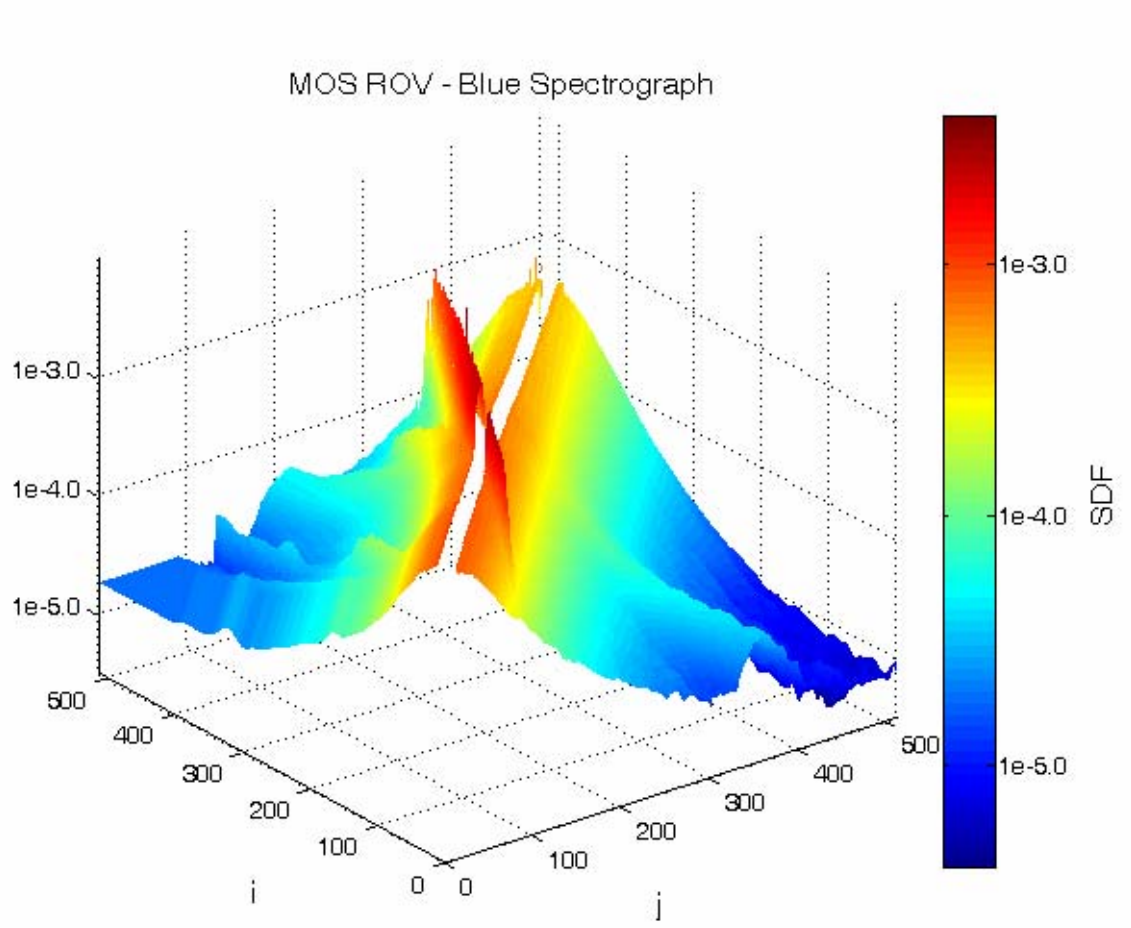

Figure 15(a). ROV full D-matrix for the Blue Spectrograph. The center pixels have been given a nominal value of 1e-6 instead of 0 for these logarithmic graphs.

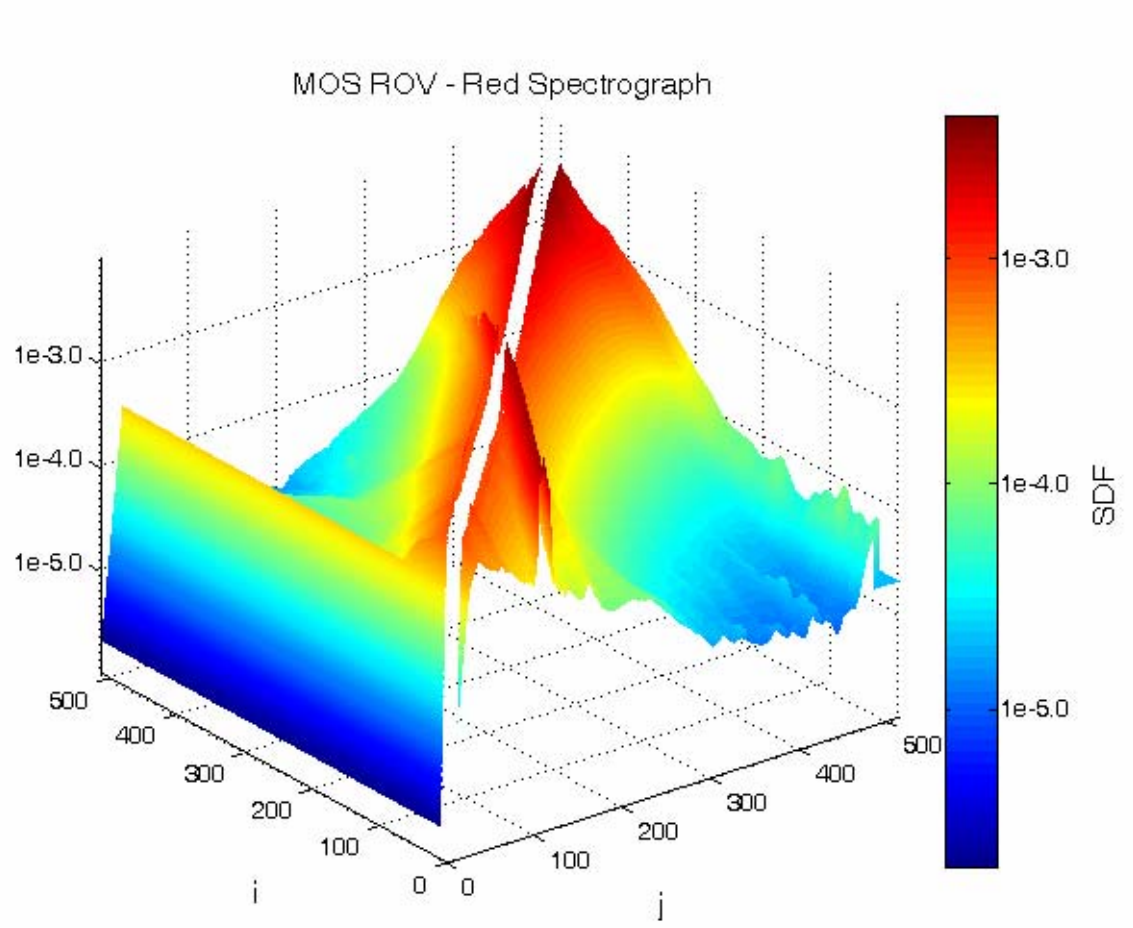

Figure 15(b). ROV full D-matrix for the Red Spectrograph. The center pixels have been given a nominal value of 1e-6 instead of 0 for these logarithmic graphs.

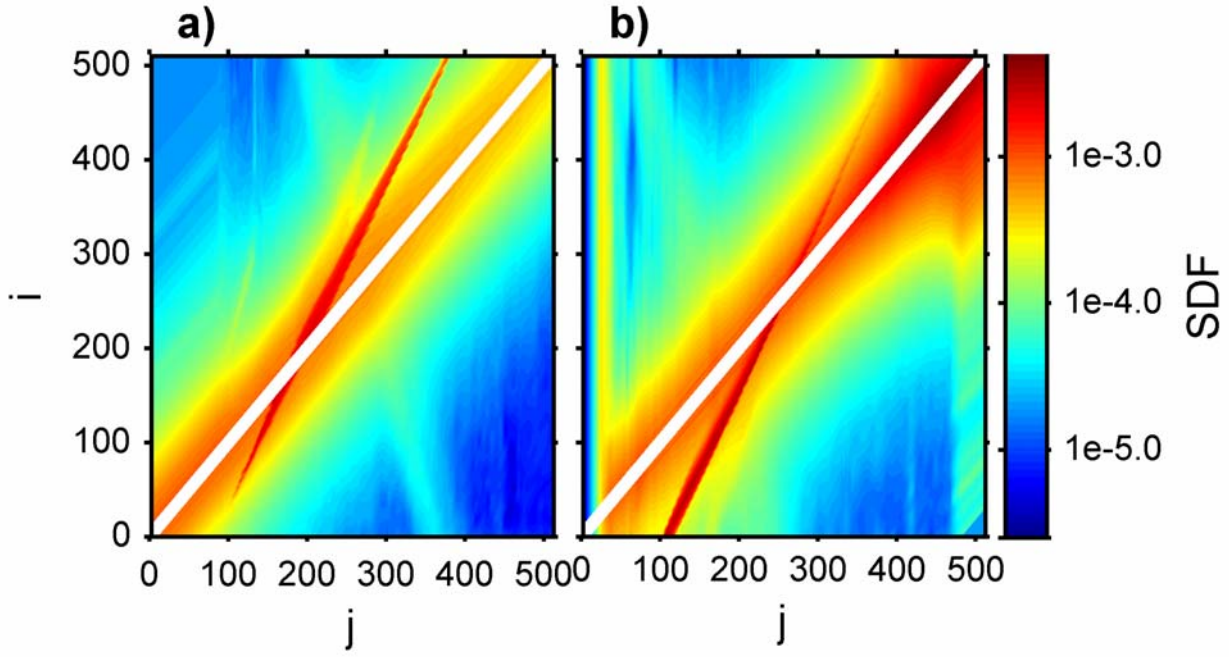

Figure 16. Top view of the D-matrix for (a) ROV, Blue Spectrograph; (b) ROV, Red Spectrograph.

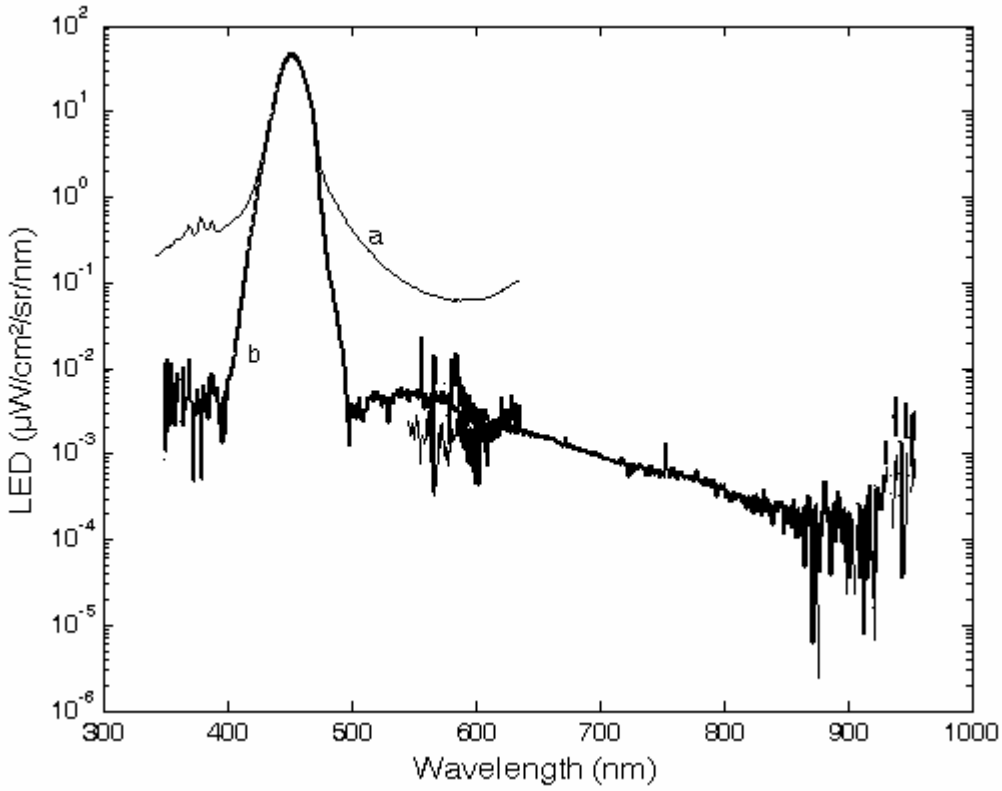

Figure 17. (a) Uncorrected and (b) stray light corrected MOS ROV measurements of a blue LED diver lamp.

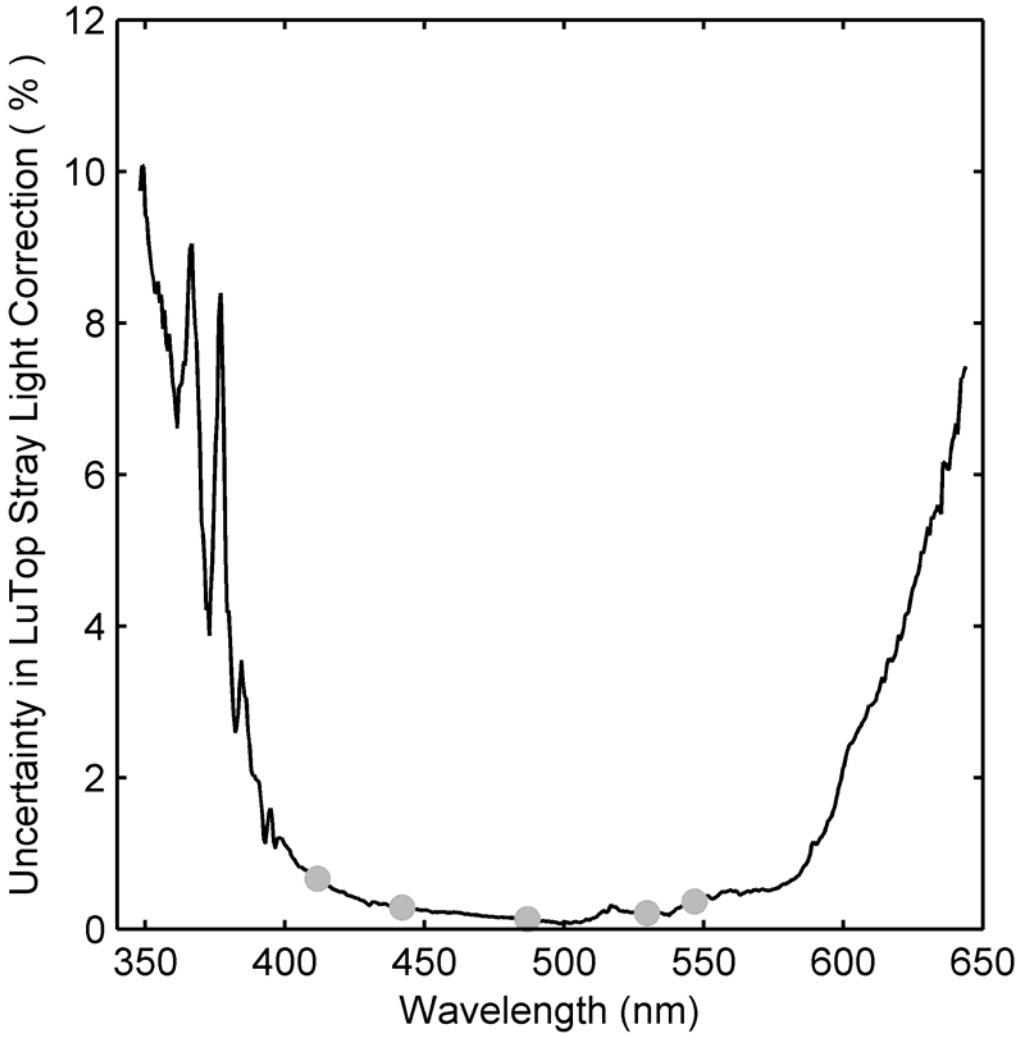

Figure 18. Results of Monte Carlo uncertainty analysis. Grey circles represent band-center wavelengths of MODIS Terra bands.

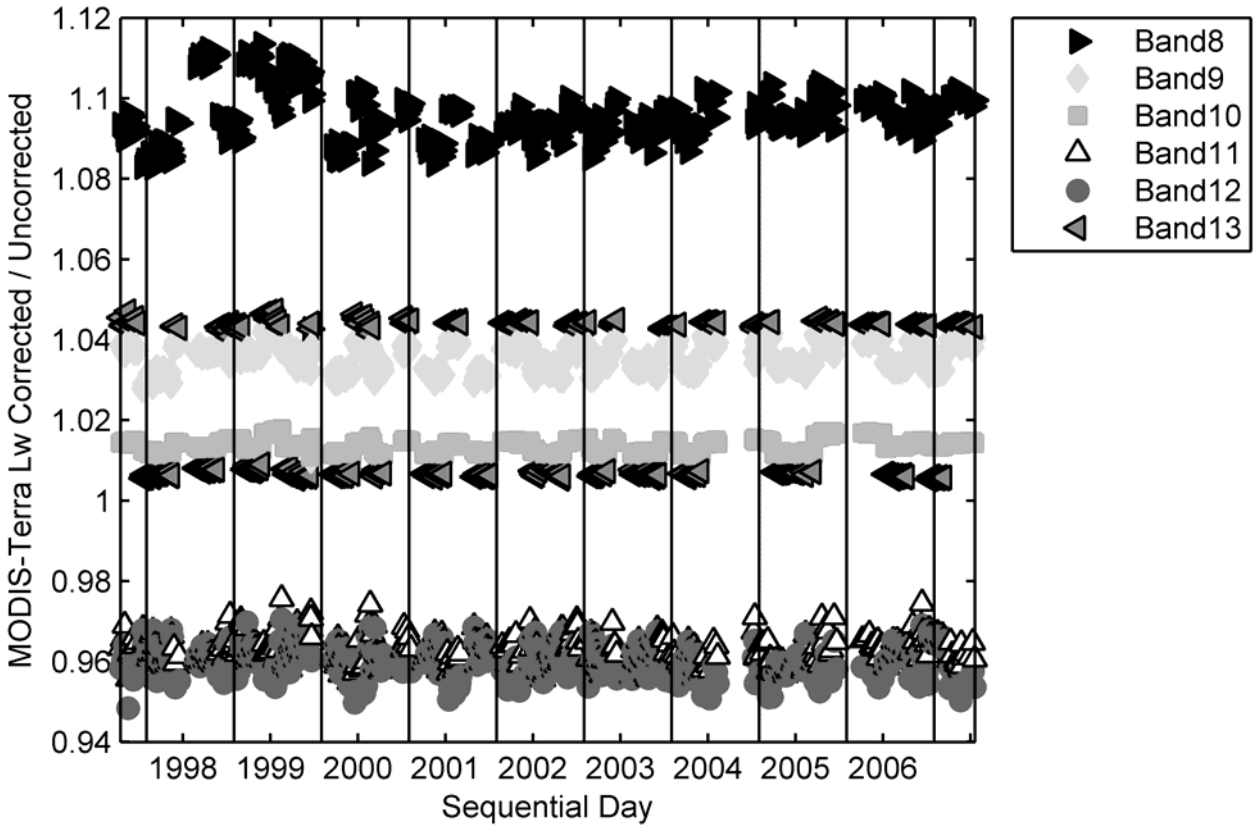

Figure 19. The ratio of stray light corrected over uncorrected water leaving radiance for MODIS Bands 8 through 13. Data show all deployments from September 1997 (deployment 3) through June 2007 (deployment 33). Data for even and odd buoys, MOS204 and MOS205, are shown.

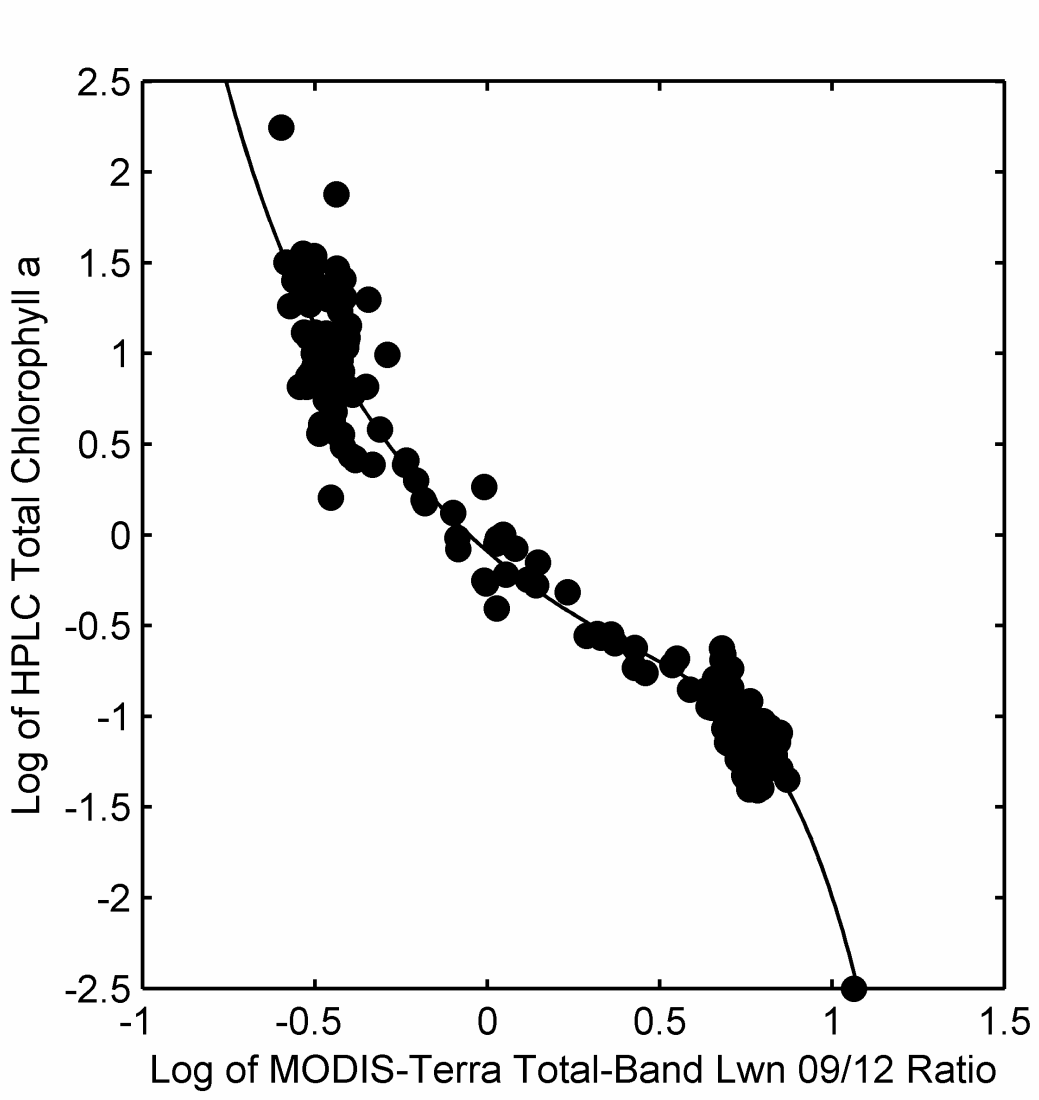

Figure 20. MODIS Terra bio-optical algorithm relating the log of HPLC-measured total chlorophyll-*a* to the log of MODIS Band 9 to Band 12 water-leaving radiance ratio. The data are shown as solid circles; the solid line is a 5th order polynomial fit to the data.

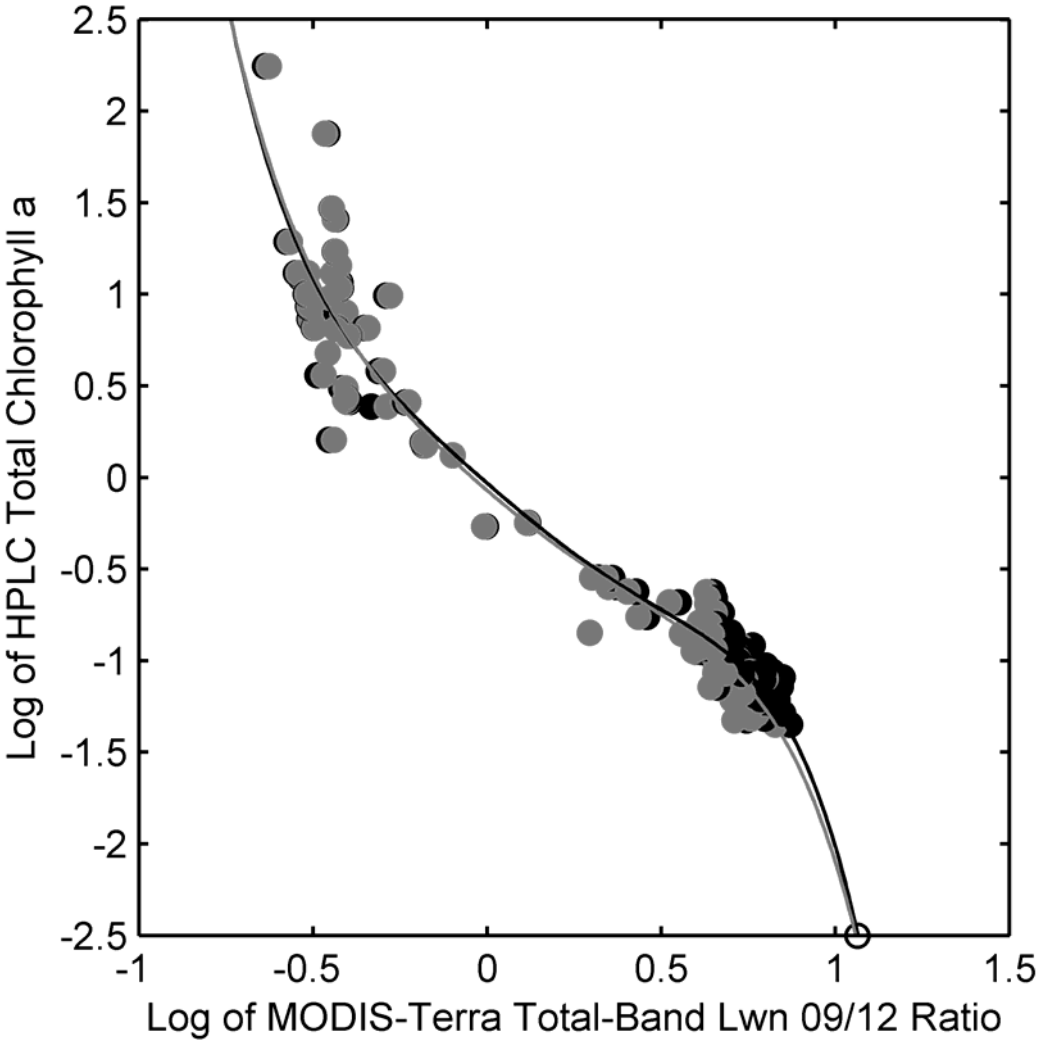

Figure 21. MODIS Band 9 to Band 12 water-leaving radiance data corrected (dark circles) and uncorrected (grey circles) for stray light. The dark and grey solid lines are 5th order, polynomial fits to the data.